

Simulations of minor mergers. I. General properties of thick disks

Álvaro Villalobos^{*} and Amina Helmi[†]

Kapteyn Astronomical Institute, University of Groningen, P.O. Box 800, 9700 AV Groningen, The Netherlands

ABSTRACT

We present simulations of the formation of thick disks via the accretion of two-component satellites onto a pre-existing thin disk. Our goal is to establish the detailed characteristics of the thick disks obtained in this way, as well as their dependence on the initial orbital and internal properties of the accreted objects. We find that mergers with 10–20% mass of the mass of the host lead to the formation of thick disks whose characteristics are similar, both in morphology as in kinematics, to those observed. Despite the relatively large mass ratios, the host disks are not fully destroyed by the infalling satellites: a remaining kinematically cold and thin component containing $\sim 15 - 25\%$ of the mass can be identified, which is embedded in a hotter and thicker disk. This may for example, explain the existence of a very old thin disk stars in the Milky Way. The final scale-heights of the disks depend both on the initial inclination and properties of the merger, but the fraction of satellite stellar particles at ~ 4 scale-heights directly measures the mass ratio between the satellite and host galaxy. Our thick disks typically show boxy isophotes at very low surface brightness levels (> 6 magnitudes below their peak value). Kinematically, the velocity ellipsoids of the simulated thick disks are similar to that of the Galactic thick disk at the solar radius. The trend of σ_Z/σ_R with radius is found to be a very good discriminant of the initial inclination of the accreted satellite. In the Milky Way, the possible existence of a vertical gradient in the rotational velocity of the thick disk as well as the observed value of σ_Z/σ_R at the solar vicinity appear to favour the formation of the thick disk by a merger with either low or intermediate orbital inclination.

Key words: methods: numerical – galaxies: formation, kinematics and dynamics, structure – Galaxy: disc, kinematics and dynamics, formation

1 INTRODUCTION

The different components of disk galaxies contain key information about various stages of the formation history of these systems. In this sense, one of the most significant components for studying signatures of galaxy formation are the thick disks because they contain imprints of the state of early disks and their interaction with the galactic environment (Freeman & Bland-Hawthorn 2002).

Until now thick-disks have been detected in S0 galaxies (Burstein 1979; Tsikoudi 1979), in the Milky Way (Gilmore & Reid 1983) and in many other spirals (van der Kruit & Searle 1981a,b; Jensen & Thuan 1982; van Dokkum et al. 1994; Morrison et al. 1997; Pohlen et al. 2000; Dalcanton & Bernstein 2002; Yoachim & Dalcanton 2006, and references therein). As such, thick disks appear to be a rather ubiquitous structural component of galaxies.

Historically, there have been two types of scenarii proposed to explain the formation of thick disks: (i) “dissipational”, and (ii) “predominantly dissipationless” models. In the first case, thick-disk stars are formed during the dissipational collapse of gas with a large scale-height, after the halo has formed and before the thin disk has completely developed. A variant of this model, more in line with modern cosmology, is given by Brook et al. (2004, 2005) and consists of the formation of the thick disk in an epoch of multiple mergers of gas-rich building blocks. In this class of models, one may expect a smooth transition between properties of the thin and thick disks (Eggen et al. 1962; Gilmore & Wyse 1986; Norris & Ryan 1991; Burkert et al. 1992; Pardi et al. 1995; Fuhrmann 2004). Evidence of such a process at work may be the chain and clumpy galaxies observed at high-redshift by Elmegreen & Elmegreen (2006), which have also been suggested to be the progenitors of thick disks (e.g. Bournaud et al. 2007a). In the “predominantly dissipationless” models the thick disk stars were either: (1) vertically “heated” from a pre-existent thin disk during a (signifi-

^{*} E-mail: villalobos@astro.rug.nl

[†] E-mail: ahelmi@astro.rug.nl

cant) minor merger (Quinn et al. 1993; Mihos et al. 1995; Walker et al. 1996; Robin et al. 1996; Velázquez & White 1999; Aguerri et al. 2001; Chen & the SDSS Collaboration 2001); (2) directly deposited at large scale-heights as tidally stripped debris during the accretion of smaller satellite galaxies (Bekki & Chiba 2001; Gilmore et al. 2002; Abadi et al. 2003; Martin et al. 2004; Navarro et al. 2004; Helmi et al. 2006); or (3) the product of the dissolution of massive thin-disk clusters with small radii and large velocity dispersions (Kroupa 2002). The first and third models have in common the presence of a pre-existing disk component. In this second class of models, the thick disk may be characterised as a completely foreign component.

Models involving either one or more minor mergers – including the case of gas-rich accretion proposed by Brook et al. – are natural in the context of current theories of hierarchical structure formation (e.g., Kazantzidis et al. 2007). Such models are also supported by modern studies of both kinematical and chemical properties of the thick disks in the Milky Way and in external galaxies (Yoachim & Dalcanton 2005, 2006; Seth et al. 2005; Mould 2005). The observed lack of vertical colour and chemical gradients, as well as the presence of counter-rotating disks, favours scenarios in which thin and thick disks formed as separate entities. However, it is unclear to what extent such models reproduce the detailed properties of observed thick disks. For example, in the dissipationless minor merger scenario, the thick disk should contain stars from both the heated thin disk and the accreted satellite. What fraction of the stars come from each constituent? If they are mostly satellite debris, one may expect a significantly metal-poor thick disk, which appears to be inconsistent with the observations reported in, e.g., Mould (2005).

It is the lack of very detailed predictions that motivates us to revisit the problem of thick disk formation. In this paper, we explore the hypothesis of the heating of a pre-existing thin disk by a single minor merger. In the scenario we envisage a new thin disk component would form from the accretion of cold gas after the merger has taken place. However, here we only study the global properties of the final merger product. In a follow-up paper we will focus on its phase-space structure with the aim of making a detailed comparison to the thick disk in the Solar neighbourhood, and eventually to uncover the debris from the object that may have triggered its formation (Villalobos & Helmi, in prep). It is important to note that we shall neglect the effect of gas on the properties of the remnant thick disk for the moment. This simplification should be borne in mind, in particular since the structure of minor merger remnants may be different, as suggested by Naab et al. (2006) and Younger et al. (2008).

Significant work has been carried out in the past to model the disk heating process by a minor merger from the numerical point of view, starting from Quinn & Goodman (1986) (QG86); Quinn, Hernquist, & Fullagar (1993) (QHF93); Mihos et al. (1995); Walker, Mihos, & Hernquist (1996) (WMH96); Huang & Carlberg (1997) (HC97); Sellwood et al. (1998); Velázquez & White (1999) (VW99), and more recently Kazantzidis et al. (2007), and simultaneously with this work Read et al. (2008). These papers have essentially shown that it is relatively easy to produce thick disks whose general properties are consistent with

those observed. However, we believe there is still room for improvement, both in the initial conditions used to model this process, as well as in the degree of detail necessary for comparisons to the latest observations of thick disks.

Besides the work mentioned above, in recent years several authors have studied minor mergers with a number of different goals (other than the formation of thick disks). These include for example, studies of the merger remnants produced by encounters between disk galaxies (as a way of producing a bulge dominated system, e.g. Naab & Burkert 2003; Jesseit et al. 2005; Naab & Trujillo 2006). More recently, also the effects of gas, star formation and feedback have been taken into account (Bournaud et al. 2005; Naab et al. 2006; di Matteo et al. 2007; Cox et al. 2008). The effects of repeated minor mergers have been considered in, e.g. Bournaud et al. (2007b); Kazantzidis et al. (2007).

The space of initial conditions to tackle the formation of the thick disk via minor mergers is very large, and it is not desirable to probe it randomly. We have therefore made the following physically motivated choices. (i) We model the formation of thick disks at two different redshifts, by scaling the properties of the host galaxy and accreted satellite according to cosmological models, as in Mo, Mao, & White (1998) (ii) We consider the accretion of relatively massive satellites (10% or 20% mass ratios), embedded in dark-matter halos, and with stellar distributions that are initially either spherical (and on the fundamental plane of dE+dSphs galaxies) or disk. (iii) The satellites are released much farther away from the host disk compared to previous studies, and their orbits are consistent with those of infalling substructures in cosmological simulations (e.g., Benson 2005).

The outline of this paper is the following: In §2 we describe in detail the numerical procedure used to build self-consistently the different components of both the host galaxy and satellites including our choices for the numerical parameters and the orbital parameters of the satellites. §3 describes the outcome of the simulations, focusing on the final properties of thick disks and the evolution of satellites. In §4 we present a discussion and limitations of our approach. In §5 we summarise the main results.

2 SETTING UP THE SIMULATIONS

In this section, we describe in broad terms the procedure adopted to model the host disk galaxy and the (to be accreted) satellite. We refer the interested reader to the Appendix for more details. We consider two configurations: a merger with a host whose properties resemble the Milky Way today (our “z=0” experiment), and a merger with a smaller host disk galaxy (this is our “z=1” experiment). The “z=0” configuration has been often used in the past in the same context (QG86; QHF93; WMH96; HC97; VW99; Aguerri et al. 2001; Font et al. 2001; Ardi et al. 2003; Hayashi & Chiba 2006). In the “z=1” configuration both the host system and the satellite’s properties are scaled to those expected at z=1 according to the model of Mo et al. (1998). In this case, the aim is to simulate the merger event that might have given rise to the Milky Way thick disk. In this configuration the mass of the present-day thick disk of the Milky Way is roughly equal to the combined mass of the host disk galaxy and the stellar component of the satellite.

Table 1. Properties of host disk galaxies.

	“z=0”	“z=1”	
NFW Halo			
Virial mass, M_{vir}	10^{12}	5.07×10^{11}	$[M_{\odot}]$
Virial radius, R_{vir}	258.91	122.22	[kpc]
Concentration, c	13.12	6.56	
Circular velocity, $V_c(R_{vir})$	129.17	133.87	[km/s]
N_H	500000	500000	
Softening, ϵ_{halo}	0.35	0.41	[kpc]
Disk			
Disk mass, M_{disk}	2.8×10^{10}	1.2×10^{10}	$[M_{\odot}]$
Scale-length, R_D	3.5	1.65	[kpc]
Scale-height, z_0	0.35	0.165	[kpc]
Toomre Q($R = 2.4R_D$)	2.0	2.0	
N_D	100000	100000	
Softening, ϵ_{disk}	0.05	0.012	[kpc]

In this section we also describe the orbital parameters of the various experiments. Furthermore, we explain the choices made for the numerical parameters employed in our simulations, and describe the global stability of the system.

2.1 Main disk galaxy

We model the main disk galaxy as a self-consistent two-component system, containing a NFW dark matter halo (Navarro et al. 1997) and a stellar disk. The dark halo is adiabatically contracted in response to the formation of a stellar disk in its central part (Blumenthal et al. 1986; Mo et al. 1998). The disk component is constructed following the procedure outlined by QHF93 and Hernquist (1993), and follows a density profile of the form:

$$\rho_d(R, z) = \frac{M_d}{8\pi R_D^2 z_0} \exp\left(-\frac{R}{R_D}\right) \operatorname{sech}^2\left(\frac{z}{2z_0}\right) \quad (1)$$

where M_d is the disk mass, R_D is the exponential scale-length, and z_0 is the exponential¹ scale-height.

Following Mo et al. (1998), the ratios M_{halo}/M_{disk} and R_{vir}/R_D have been kept nearly constant for all redshifts. The scale-height z_0 has been kept as $0.1R_D$ according to observations of external galaxies (Kregel et al. 2002). This has also been assumed in our “z=1” experiments. By keeping this ratios constant, the way in which the mass and dimensions of the disk component scale with redshift is simplified, since it follows the same scaling with redshift as the halo within which it is embedded. The chosen values for the parameters of the main disk galaxy are listed in Table 1 for our “z=0” and “z=1” experiments.

2.2 Satellite Galaxies

The satellite galaxies are designed self-consistently with both dark matter and stellar components. The dark halo follows a NFW density profile, and the initialisation procedure is identical to that for the host system.

¹ Note that $\operatorname{sech}^2(z/2z_0) \approx \exp(-|z|/z_0)$ for $|z| \gg z_0$.

Table 2. Properties of satellite galaxies.

	“z=0”	“z=1”	
NFW Halo			
Virial mass, M_{vir}	2×10^{11}	1.01×10^{11}	$[M_{\odot}]$
Virial radius, R_{vir}	151.40	71.35	[kpc]
Concentration, c	16.18	8.09	
Circular velocity, $V_c(R_{vir})$	75.50	78.10	[km/s]
N_H	100000	100000	
Softening, ϵ_{halo}	0.14	0.07/0.14 ¹	[kpc]
Disk			
Disk mass, M_{disk}	5.6×10^9	2.4×10^9	$[M_{\odot}]$
Scale-length, R_D	1.69	0.96	[kpc]
Scale-height, z_0	0.17	0.095	[kpc]
Toomre Q($R = 2.4R_D$)	2.0	2.0	
N_D	100000	100000	
Softening, ϵ_{disk}	0.024	0.007	[kpc]
Bulge			
Bulge mass, M_{bulge}	5.6×10^9	2.4×10^9	$[M_{\odot}]$
Scale radius, a_b	0.9	0.709	[kpc]
Velocity dispersion, σ_0	96.29	69.06	[km/s]
N_B	100000	100000	
Softening, ϵ_{bulge}	0.07	0.07	[kpc]

¹: Softenings used in diskly and spherical satellites respectively.

We consider two possible stellar distributions: an exponential disk and a spherical Hernquist bulge. In this case, the density is given by (Hernquist 1990):

$$\rho_b(r) = \frac{M_b}{2\pi} \frac{a_b}{r(r+a_b)^3} \quad (2)$$

where M_b is the bulge mass and a_b is the scale radius.

Both types of satellites satisfy $M_{total,sat} = 0.2M_{total,host}$ for the “z=0” and “z=1” experiments. In particular, the mass ratio between dark matter and luminous matter in the satellites is set to be the same as in the host galaxy. This implies that the mass of the stellar components of our satellites is 20% of $M_{disk,host}$, similar to those adopted in previous work on disk heating by satellite accretion (QHF93; WMH96; HC97; VW99). Note however that the initial total mass of the satellite is comparable to that of the host disk. For completeness, we also include the case of a satellite with a stellar mass of 10% of $M_{disk,host}$. In this case the total mass of the satellite is also 10% of that of the host galaxy.

The spherical satellites lie on the observed fundamental plane of dE+dSphs galaxies (de Rijcke et al. 2005):

$$\log L_B \sim 4.39 + 2.55 \log \sigma_0 \quad (3)$$

$$\log L_B \sim 8.65 + 3.55 \log R_e \quad (4)$$

where L_B is the blue-band luminosity, and σ_0 is the central velocity dispersion. The effective radius is related to the scale radius by $R_e \approx 1.82a_b$ for a Hernquist density profile. Finally, we fix the mass-to-light ratio $\Upsilon_B = 2\Upsilon_{B_{\odot}}$ to derive the stellar mass of our spherical satellites.

The structural parameters of the diskly satellites, R_D and z_0 are set in the same way as for the host.

The above relations fully specify the properties of our satellites, both for the “z=0” and “z=1” experiments. Note

that the variation with redshift is always linked to that of the host halo. Table 2 lists the properties of both spherical and disk satellites for “z=0” and “z=1”.

2.3 Orbital Parameters

We release our satellites from significantly larger distances than previous works (e.g., QG86; VW99; Kazantzidis et al. 2007). For the “z=0” case, the satellite is launched from the virial radius of the host galaxy computed at z=1 ($R_{vir} = 122.22$ kpc $\approx 35R_D$). For the “z=1” experiment, it is launched from a distance of 83.9 kpc ($\approx 50R_D$) which corresponds to the virial radius of the host galaxy computed at z=1.6.

To initialise the orbital velocities of the satellites, we follow Benson (2005). Benson determined the orbital parameters of DM substructures at the time they crossed the virial radius of their host halos (see also Tormen 1997; Khochfar & Burkert 2006). We choose for the velocities of our satellites the most probable values of the distributions as given for z=0 (since little variation is visible as a function of redshift). The radial and tangential velocity distributions peak, respectively, at 0.9 and 0.6 in units of $V_c(R_{vir})$.

We consider for our satellites initial orbital inclinations of 0°, 30° and 60° (with respect to the plane of the host disk), in both prograde and retrograde directions with respect to the rotation of the host disk. In the case of disk satellites, their midplanes are parallel to that of the primary disk, implying that they are, respectively, inclined by 0°, 60° and 30° with respect to their orbital planes. Table 3 summarises the orbital parameters adopted for both spherical and disk satellites, for the configurations at “z=0”, and “z=1”.

Note that within each configuration, all the satellites are initially released from the same distance with the same velocity modulus, i.e., they all have the same total energy and modulus of the angular momentum, but the latter varying its orientation. This implies that the initial apocentre, pericentre (and hence orbital eccentricity) are the same for all experiments. However, as we shall see in §3.1 the orbits evolve due to dynamical friction, with some dependence on the internal properties of the satellite. Therefore, at the time the satellite merges with the disk, the orbits of all our experiments are different.

With these initial conditions, we find that our satellites have completely merged with the host disks by $z \approx 0.4$ and by $z \approx 1$, respectively for the “z=0” and “z=1” cases.

2.4 Numerical Parameters

The N -body systems are evolved using Gadget-2.0 (Springel 2005) a well documented massively parallel TreeSPH code. Our choices of the numerical parameters (number of particles N in each component in the system; softening ϵ and timestep Δt) are described in detail in §A2. Tables 1 and 2 list the values used for each component in our simulations. The maximum timestep (not listed in the Tables) is 0.25 Myr. Typically the energy and angular momentum are conserved to better than 0.1% over 9 Gyr of evolution for our main disk galaxy configured at “z=0”.

Table 3. Initial orbital parameters of satellite galaxies.

i	x	z	v_x	v_z	L_z
“z=0”					
0°	122.2	0.0	-137.7	0.0	11219.8
30°	105.8	61.1	-119.2	-68.8	9716.6
60°	61.1	105.8	-68.8	-119.2	5609.9
“z=1”					
0°	83.9	0.0	-118.2	0.0	6615.9
30°	72.7	42.0	-102.4	-59.1	5729.5
60°	42.0	72.7	-59.1	-102.4	3307.9

NOTES:

- Distances in kpc, velocities in km/s, angular momentum in kpc×km/s.
- In all cases, $y = 0$ kpc, and $v_y = 91.8$ km/s for “z=0” and $v_y = 78.8$ km/s for “z=1”.
- Listed v_y and L_z are for prograde orbits. Retrograde orbits have the opposite sign.
- Initially $r_{apo} = 77$ kpc and 49 kpc, $r_{peri} \sim 10$ kpc and 5 kpc, respectively for the “z=0” and “z=1” configurations (as measured from the first apocentre and the subsequent pericentre). The corresponding eccentricities $e = (r_{apo} - r_{peri}) / (r_{apo} + r_{peri})$ are 0.77 and 0.82.

2.5 Evolution of Isolated Host Galaxy

Before including the satellite, the host galaxy is simulated in isolation to test its stability in the absence of any external perturbation. As we show in §A3 our host galaxies are very stable in their properties (cf., VW99; Gauthier et al. 2006) for the amount of time needed to complete the experiments. Therefore, we are now ready to focus on how these systems evolve when they suffer a minor merger.

3 RESULTS

In total, 25 simulations have been carried out to study the formation and global properties of thick disks as a result of the merger between a host disk galaxy and a satellite. The simulations explore combinations of the following elements: two configurations for the progenitors (“z=0” and “z=1”); two morphologies for the stellar component of the satellite (spherical and disk); two total mass ratios between the satellite and the host galaxy (10% and 20%); and three initial orbital inclinations for the satellite with respect to the midplane of the host disk (0°, 30° and 60°), in both prograde and retrograde directions.

3.1 Orbital Evolution of the Satellites

To study the evolution of the orbits in our experiments we follow the location of the centre of mass of the satellite (CM) with respect to the host galaxy. The CM is defined as the mean position of bound stellar and DM particles of the satellite. Fig. 1 shows the trajectories of the CMs for the experiments configured at “z=0” and “z=1” with a spherical satellite on a prograde orbit with initial inclination $i = 30^\circ$. The XY projections clearly illustrate how radial the orbits

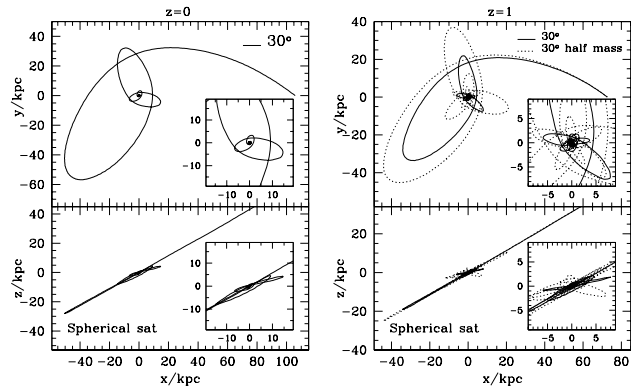


Figure 1. XY and XZ projections of the trajectory of the centre of mass of a spherical satellite as it decays towards the centre of the host galaxy in our “ $z=0$ ” and “ $z=1$ ” experiments with initial inclination 30° . The coordinate system is centred on the centre of mass of the host disk. The inset panels show in more detail the trajectory of the satellite at late times before it is fully disrupted.

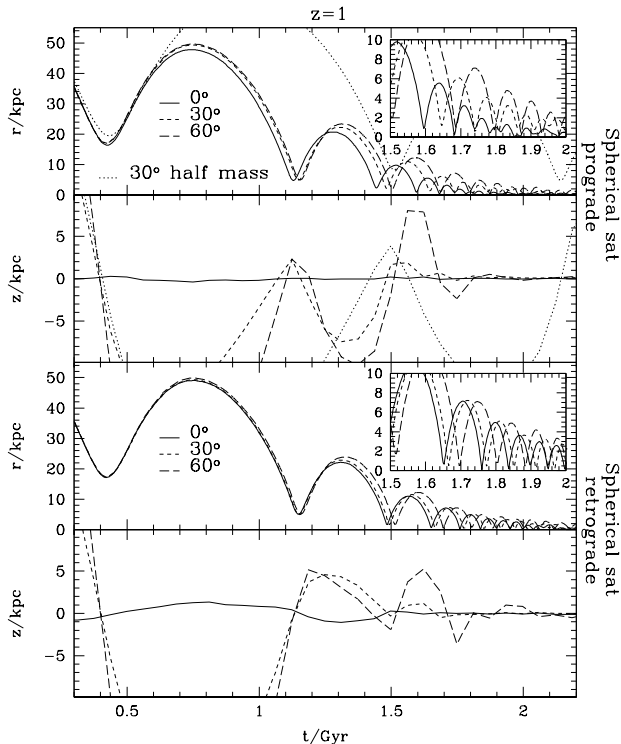


Figure 2. Evolution of the radial separation between the centres of mass of the host disk and the satellite, and of the z -distance of the satellite’s centre of mass with respect to the host disk plane, for spherical satellites on prograde (top panels) and retrograde (bottom panels) encounters. The various curves correspond to different orbital inclinations for the “ $z=1$ ” configuration, and the 10% experiment is shown for the inclination of 30° . The insets show in more detail the trajectory of the satellites at late times. The lack of a clear trend in the amplitude of the vertical oscillations is likely due to the difficulty in determining the exact orientation of the disk plane at the ~ 1 kpc level. Similar behaviours are observable for the “ $z=0$ ” case.

are and how rapidly they decrease in amplitude due to dynamical friction between the satellite and the host system. Note that these orbits are quite different from the circular ones usually used in earlier studies (e.g., QG86; QHF93; WMH96). The XY and XZ projections show that the satellites stay on their original orbital planes as they decay, until they enter into the zone dominated by the host disk, when they are drawn onto the disk plane and spiral in towards its centre. This is particularly clear for the lighter satellite in our “ $z=1$ ” experiment that spends ~ 1 Gyr on the disk plane before sinking in further.

Note that most of the angular momentum of the “satellite + host system” is in the orbital motion of the satellites. This is because the satellites are relatively massive and have a very large initial distance from the host. As a result, when the satellite decays in an inclined orbit the disk is strongly tilted in both the prograde and retrograde cases (see §3.3).

As expected, the trajectory of the lighter satellite is more extended because dynamical friction is less efficient in this case (Binney & Tremaine 1987). Our 20% satellites decay completely after ~ 3 Gyr in the case of “ $z=0$ ” experiments, and after ~ 2 Gyr for “ $z=1$ ” experiments. In comparison, the satellite with half of the mass takes the double of time to sink starting from the same initial orbital parameters.

Initially, the orbital decay is due to the dynamical friction against the host halo. This implies that the decay rate does not depend on inclination, orbital direction or stellar mass distribution (see Fig. 2). On the other hand, when the satellites approach the centre of the system (where the disk is a significant contributor to the global force field), the orbit decays by dynamical friction also against the host disk. Thus at later times, prograde low inclination orbits decay faster than retrograde or high inclination orbits (QG86; WMH96; see also HC97).

3.2 Satellite Mass Loss

Fig. 3 shows the mass loss evolution of both DM and stellar components of spherical and disky satellites in the “ $z=0$ ” and “ $z=1$ ” experiments.

In order to calculate how much mass remains bound to the satellite at a given time we implemented in Gadget-2.0 the following procedure (Benson et al. 2004):

- (i) Start by considering all the satellite particles that were bound to the satellite at the previous timestep (or simply all satellite particles for the first timestep).
- (ii) Compute the mass of the satellite from these particles along with the position and velocity of the CM.
- (iii) For each particle in this set, determine whether it is gravitationally bound to the other particles in the set.
- (iv) Retain only those particles that are bound and go back to step (ii). Repeat until the mass of the satellite has converged.

Since the satellites were initialised in the absence of an external potential, as soon as they are placed within the host potential a large fraction (70%) of the more extended DM component rapidly becomes unbound before the first pericentric passage. After that, the mass loss rate of the DM component mostly depends on its initial mass.

The mass loss rate of the stellar components depends

strongly on initial mass, and orbital parameters (WMH96; HC97; VW99) but also on the stellar mass distribution. As satellites decay, prograde orbits with lower inclinations lose mass faster than retrograde orbits with higher inclinations, due to the stronger tidal interaction with the host galaxy. This trend is more notorious for disk satellites. Spherical satellites are also characterised by a more extended “knee” in the mass loss in comparison to disk satellites. The lighter satellite experiences a slower mass loss compared to heavier satellites, because it suffers less dynamical friction and hence is on a less bound orbit.

Once a satellite has sunk onto the plane of the host disk, its fate will depend on its instantaneous mean density compared to the mean density of the host at a given location. If the mean density of the satellite is larger than that of the host system then the most bound particles of the satellite will reach the galactic centre as a distinctive core causing more damage to the host disk. Otherwise, the satellite will receive most of the damage, being heated and torn apart by the host disk. In our simulations only the mergers with spherical satellites in the “ $z=0$ ” experiments deposit in the galactic centre final cores of up to 20% the initial stellar mass. These final cores are on the lighter side in comparison with previous studies using high density satellites (QHF93, 20%; WMH96, 45%). It is interesting to note that spherical satellites with higher inclinations give rise to the formation of less massive cores. This can be explained by the fact that satellites on higher inclinations experience more disk crossings through the host disk as they decay, compared to ones on lower inclinations. In this case disk shocks perturb the structure of the satellite and cause additional mass loss (see Binney & Tremaine 1987; QHF93).

Figure 3 shows that in general most of the dark matter is stripped off early, and deposited at very large radii (see Fig. 2). Therefore the fraction of dark matter accreted from the satellite and deposited in a disk-like structure is very small in our simulations, in comparison to what Read et al. (2008) find. This may be explained by the fact that our satellites, although of comparable mass, are launched from much larger distances.

3.3 Description of the Mergers

Figure 4 illustrates the morphological changes in the host disk during merger events configured at “ $z=1$ ”. The initial inclination of the satellite is 30° for both prograde and retrograde orbits.

As the satellite decays in its orbit, it induces the formation of noticeable spiral arms in the host disk, which transport angular momentum from the central parts towards the outskirts. Once the satellite sinks onto the plane of the host disk it transfers kinetic energy from its orbit to the particles in the disk, increasing their vertical motions and causing a visible thickening. At the same time the disk responds to the decaying satellite, by tilting its plane in order to conserve the total angular momentum of the system (although a significant amount of the satellite’s initial angular momentum has by this time, already been transferred to the host halo).

Figs. 5 and 6 show the distribution of stellar particles for both spherical and disk satellites on prograde orbits with initial inclination 30° . In the early stages of the orbital decay, the satellite is stripped leaving trails of particles on

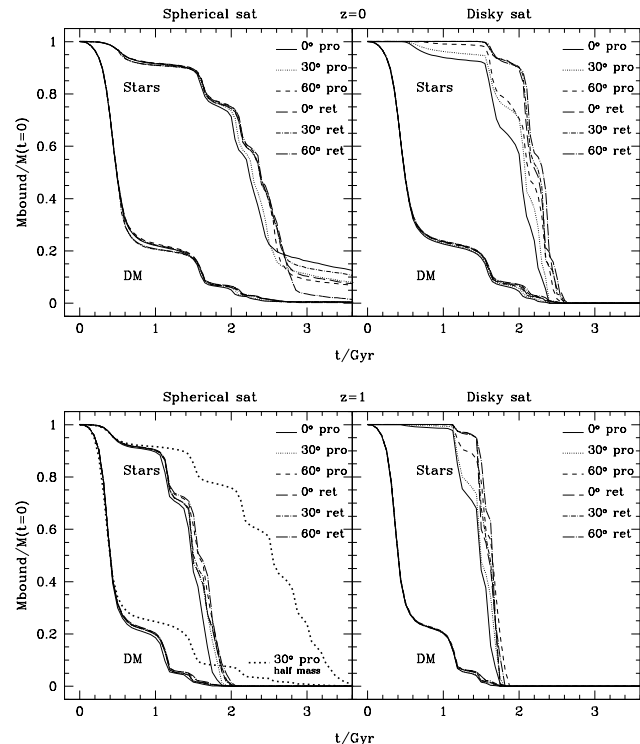


Figure 3. Mass that remains bound for both the dark matter and stellar components of the satellites in our experiments at “ $z=0$ ” (upper panels) and at “ $z=1$ ” (bottom panels). The bound mass is in units of the initial mass of the corresponding component.

orbits with inclinations similar to that of the satellite initially. Since the stars are initially deeply embedded in the satellite’s dark matter halo, only a small fraction of the stellar debris is deposited at large radii. Most of the stars from the satellite end up in a disk-like configuration, with the same orientation as the final disk, but one that is somewhat thicker and more extended (see §3.4). Noticeable shells of debris material are formed as time goes by. These structures are a consequence of the interaction of a dynamically cold system with a larger one (Hernquist & Quinn 1988). In general the survival of these shells will depend on the mean phase-space density of the infalling satellite and also on its orbit. In the case of spherical satellites shells are visible typically since $t \sim 1.7$ Gyr, lasting ~ 2 Gyr; and for disk satellites much sharper shells are seen starting at $t \sim 1.5$ Gyr, being still noticeable by the end of the simulation, i.e., ~ 2.5 Gyr later. Shells are rather common features related to merger events, being observed in many elliptical and spiral galaxies. An important characteristic of shells is that they usually survive for a long time in physical space, as previous numerical studies have shown (e.g. Hernquist & Quinn 1988, 1989). The presence of such a structures in the solar vicinity and the possible signatures imprinted on them during the formation of the thick disk will be explored in Paper II (note that such features have already been proposed to explain the Monoceros ring, see e.g. Helmi et al. 2003).

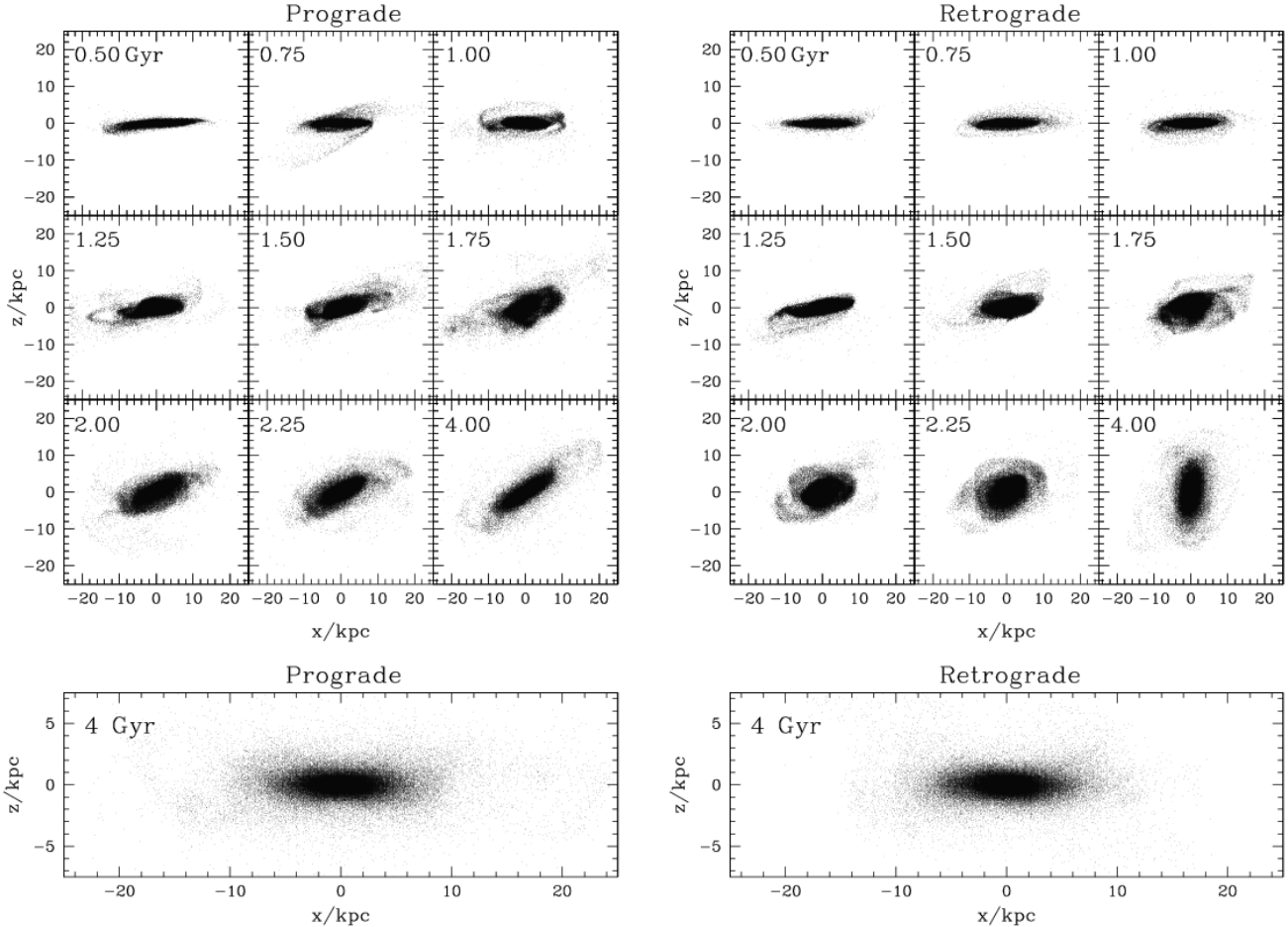


Figure 4. Evolution of the host disk (initially shown edge-on) during the merger with a spherical satellite with inclination of 30° for prograde and retrograde orbits in the “ $z=1$ ” experiment. Only host disk particles are shown for clarity. Note that the disk appears overthickened or distorted because of projection effects, especially in the case of the retrograde orbit. The bottom panels show edge-on views of the final system.

3.4 Properties of the merger products

By the end of the simulations the morphological, structural and kinematical properties of the heated disks and satellite debris have settled down and do not evolve further. This occurs ~ 2 Gyr after either the satellite has been disrupted or its core has reached the centre of the host disk. This means that the properties of the final thick disks do not change after $t=5$ Gyr and $t=4$ Gyr for the systems configured at “ $z=0$ ” and at “ $z=1$ ” respectively, in the case of heavy satellites. This timescale is ~ 6 Gyr for the lighter satellite in our “ $z=1$ ” experiment.

We now study in more detail the characteristics of the final disks. To this end we use a reference frame centred on the centre of mass of the final product, and aligned with its principal axes in such a way that the rotation axis defines the z -direction.

3.4.1 Morphological properties

The left panels in Fig. 7 show the morphologies of the heated host disks at the final time of the “ $z=1$ ” experiments ($t=4$ Gyr), for the case of the spherical satellites. Prograde orbits

and lower inclinations induce on the host moderate arms and more radial expansion in comparison with retrograde orbits and higher inclinations. On the other hand, higher prograde inclinations are more efficient at thickening the disk, especially in the outskirts. For instance, a prograde satellite with inclination of 60° only causes a slight increment of the radial extension compared to the coeval control disk, but induces a noticeable thickening compared to the same control disk and to the other inclinations. Satellites on retrograde orbits have a similar thickening effect on the disk but a considerably milder influence on the formation of tidal arms and radial expansion compared to satellites on low inclination prograde orbits. Notice also that the satellites during their decay can induce the formation of weak bars (see also Berentzen et al. 2004). Some warping in the disks is also visible in the case of mergers with inclinations of 60° for both prograde and retrograde orbits (see also QHF93; VW99).

The panels on the right side of Fig. 7 show the thick disks obtained, now including the contribution of the satellite’s stellar particles. Their final structure is dominated by the heated disk (compare to the left panels), except in the outer regions, where the contribution of satellite debris is important. The outskirts are clearly thicker for satellites on

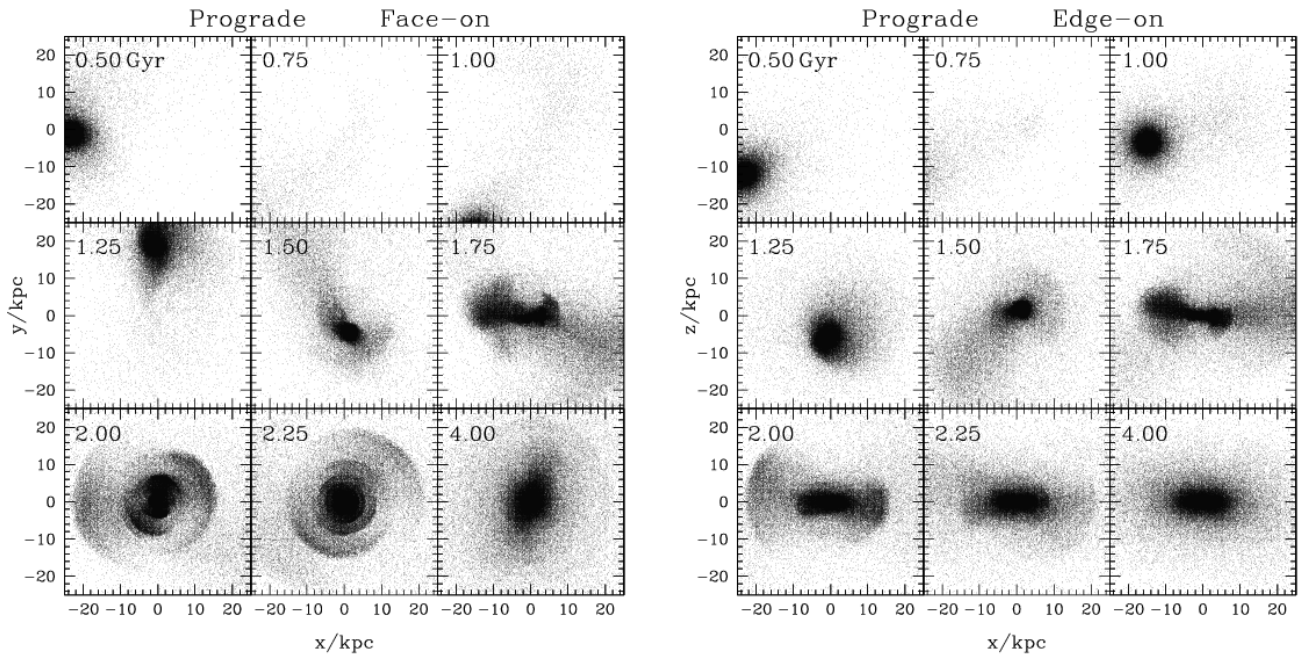


Figure 5. Evolution of the spherical satellite with inclination 30° during the prograde merger with the host galaxy in the “ $z=1$ ” experiment. In each snapshot the reference frame has been centred on the centre of mass of the host disk and has also been rotated to eliminate the tilting of the whole system with respect to the original frame. The labels *face-on* and *edge-on* are relative to the host disk (not shown here for clarity).

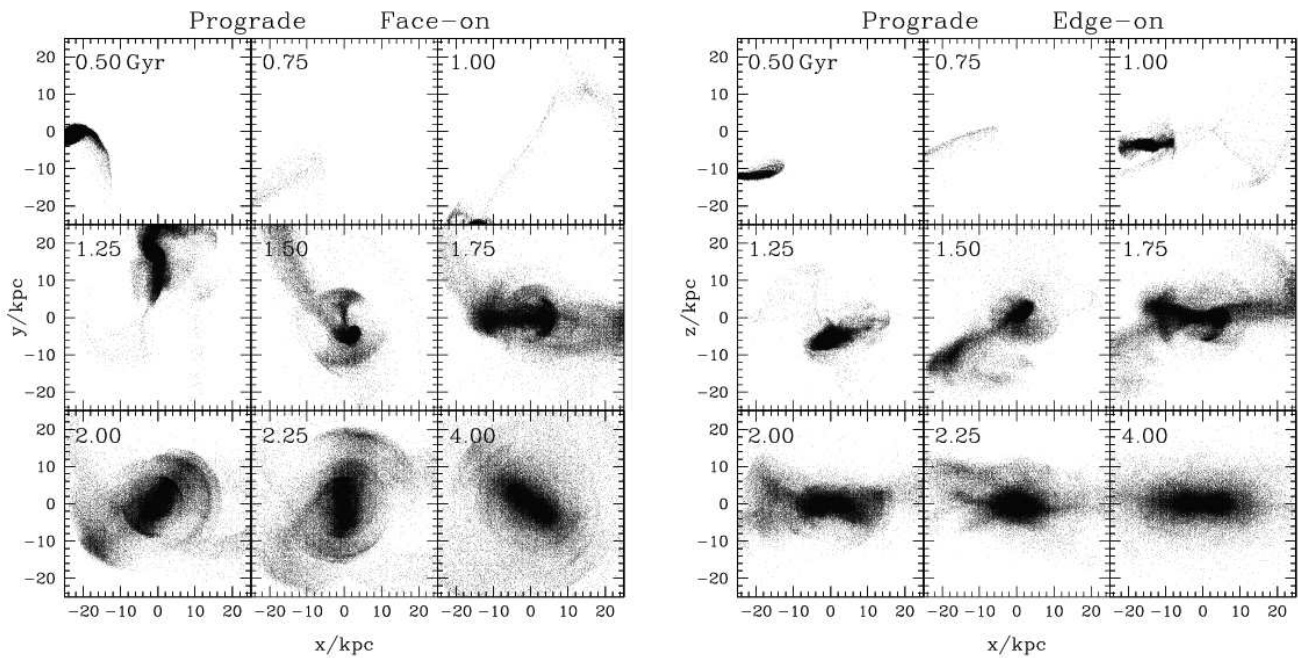


Figure 6. Same as Fig. 5, for the case of the disk satellite.

higher inclination orbits, although their debris does not show the warp feature characteristic of the heated disks. Also noticeable is the difference in the distribution of satellite debris between prograde and retrograde orbits for the case of coplanar infall (in edge-on views).

The contour levels shown in this figure have been drawn 4.5, 6.2, 8 and 9.7 magnitudes below the central surface brightness of the remnant system. If we assume a mass-to-light ratio $\Upsilon_V = 2\Upsilon_{\odot,V}$ for the host as well as for the

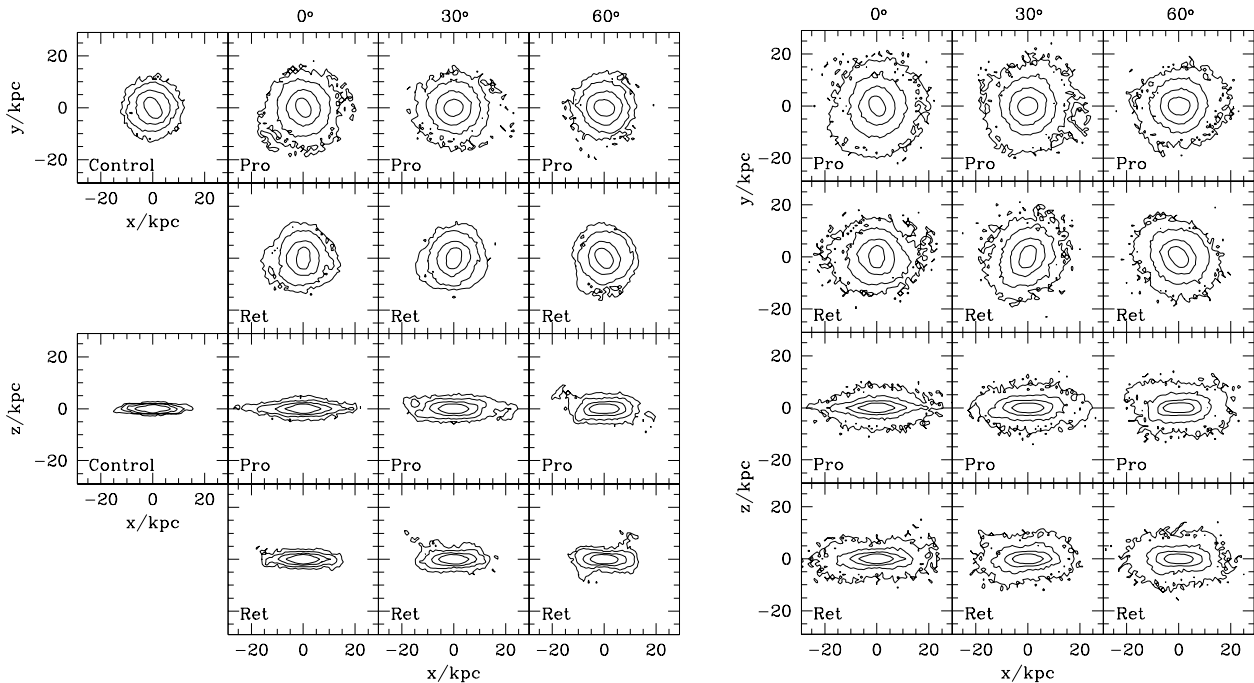


Figure 7. Face-on and edge-on views of the final morphologies of heated disks (left) and thick disks (right) at the end of the simulations in “z=1” experiments, 4 Gyr after the infall of the spherical satellite. In each case the tilting induced by the satellites has been eliminated to facilitate the comparison with the coeval control disk. The contours correspond to 4.5, 6.2, 8 and 9.7 magnitudes below the central surface brightness of the remnant system. For the experiments shown here, and assuming a mass-to-light ratio $\Upsilon_V = 2\Upsilon_{\odot,V}$, these would be located at 22.5 mag/arcsec² (innermost), 24.2 mag/arcsec², 26 mag/arcsec² and 27.7 mag/arcsec² (outermost) in the V-band.

satellite stars, these contours correspond to 22.5, 24.2, 26 and 27.7 mag/arcsec² in the V-band, respectively.

It is useful to compare this to the sample of late-type edge-on galaxies observed by Dalcanton & Bernstein (2000) (their Fig. 3) and Dalcanton & Bernstein (2002) (DB02, their Fig. 1), who typically probe up to ~ 5 mag below the central surface brightness of their (thin + thick) disks in the R-band. Their faintest contour would be located in between the first and second brightest contours shown in the right panels of Fig. 7. At least qualitatively, the surface brightness distribution of the remnants in our simulations resemble those observed by these authors.

We further quantify the shapes of the isophotal contours of the remnants by obtaining their photometry with the task ELLIPSE (Jedrzejewski 1987) of the data reduction package IRAF². This task draws an ellipse to approximately match an isophote and then expands the intensity along the ellipse as a Fourier series. According to Bender et al. (1988), the most significant non-zero component of this Fourier analysis is the a_4 parameter (corresponding to the $\cos(4\theta)$ term). Isophotes are then characterised as either disky ($a_4 > 0$) or boxy ($a_4 < 0$).

To mimic the observations, we have created artificial images out of the simulated thick disks from an edge-on point of

view, by binning a central area ($\sim 15 \times 15$ scale-lengths of the initial primary disk) into 1024×1024 pixels. When running ELLIPSE on these images, we have allowed the geometric centre, ellipticity and position angle of the isophotes to vary freely, taking linear steps of 5 pixels along the semi-major axis. We have also made sure that our results are robust to the initial guesses for the values of the various parameters required by ELLIPSE.

The left panel of Fig. 8 shows the a_4 parameter as a function of isophotal surface brightness in the V-band for our “z=1” experiments. To avoid cluttering only experiments with spherical satellites on prograde orbits are explicitly shown. The rest fall in the region delimited by the dashed envelopes. This figure shows that the isophotes go from more disky at higher surface brightness (i.e. in the central regions) to more boxy at lower surface brightness, presenting a mild trend with initial inclination of the satellite.

DB02 performed a similar analysis on their sample (see their Fig. 11). They find that inner isophotes with a surface brightness level of ~ 3 mag below the typical peak level for their sample (21 mag/arcsec²) are disky, while outer isophotes (defined as those ~ 5 mag below the peak) are as likely to be boxy as disky³. Similarly to DB02, in the right panel of Fig. 8 we plot the distribution of a_4 (weighted

² IRAF is distributed by the National Optical Astronomy Observatories, which are operated by the Association of Universities for Research in Astronomy, Inc., under cooperative agreement with the National Science Foundation.

³ It is important to keep in mind that DB02 use a different procedure to quantify the isophotal shape, meaning that the values of their shape parameters are not directly comparable to ours.

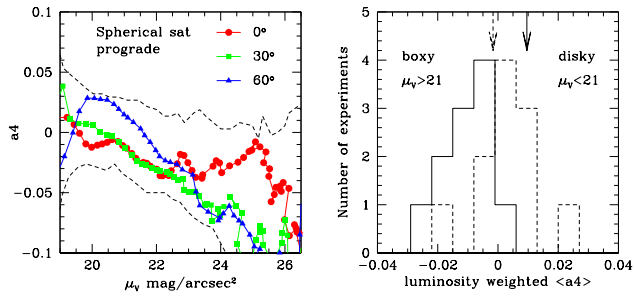


Figure 8. *Left:* a_4 vs surface brightness in the V-band for our “ $z=1$ ” experiments of a spherical satellite on a prograde orbit. The dashed curves delimit the region where all experiments fall into. Note that the central surface brightness of our remnant disks are $\mu_{V,0} \sim 18 - 19$ mag/arcsec². *Right:* Luminosity weighted distribution of the a_4 parameter for all our “ $z=1$ ” experiments. The dashed histogram corresponds to the a_4 obtained by considering the region enclosed within an isophote with $\mu < \mu_0 + 3$, while the solid one to $\mu_0 + 8 > \mu > \mu_0 + 3$. The arrows show the values of $\langle a_4 \rangle$ for the coeval control simulation.

by both errors and luminosity) for both inner and outer regions including all the “ $z=1$ ” experiments. The inner region is defined to be within 3 mag from the peak surface brightness, as done by DB02. The outer region extends down to 8 mag below the central surface brightness value. This figure confirms that inner isophotes are disk-like while outer ones appear clearly boxy. This may suggest that deeper photometry, beyond the limit reached by DB02 would be needed to detect the predominantly boxy shape of the contours in the outskirts of our remnants.

The boxy nature of the outer isophotes, which is present in all our experiments, could in principle be used as a discriminant for the formation of thick disks via mergers such as those studied here. However, it should be borne in mind that the degree of boxiness in the remnants also depends on the initial structure of the host system. For example, studies which have a spherical centrally concentrated core component (bulge or cored dark matter profile), produce a remnant which is less boxy (Naab & Burkert 2003; Bournaud et al. 2005). This is because such spherical components act in a stabilising sense for the disk (VW99; Kazantzidis et al. 2007), which therefore retains more closely its original morphology. This would imply that boxy isophotes are not necessarily direct evidence in support of the scenario proposed in this paper, but that they should be more prominent in the thick disks present in bulgeless galaxies.

3.4.2 Structural Properties

We now describe in detail the structural properties of the remnant systems produced in our experiments. We first address their vertical structure and show explicitly the need to include two components (thin and thick). We then use the information obtained from the vertical decomposition to characterise the radial extension of both disk components. Finally, the spatial distribution of stars from both the primary disk and the satellite are compared.

Note that, as mentioned above, before measuring the disks, these have been properly centred and aligned, so the

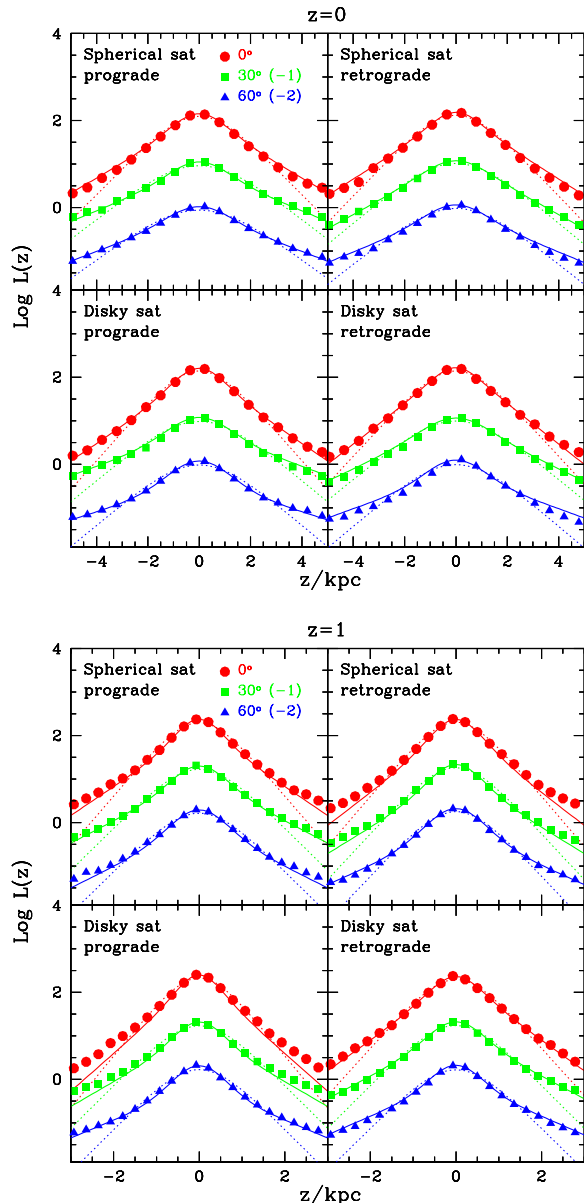


Figure 9. Vertical luminosity profiles (integrating over all radii at each height) for each of our experiments. Fits using only one component (dotted lines) systematically underestimate the luminosity far from the midplane. Two-component fits (solid lines) are clearly a better representation of the vertical structure of our remnant disks. Note that, for clarity, profiles of inclinations of 30° and 60° include offsets of $\log(L) - 1$ and $\log(L) - 2$, respectively.

rotation axis defines the z -direction. Furthermore, all the properties have been computed taking into account star particles from both the host disk and the satellite. Their relative contribution has been appropriately weighted according to the initial $M_{\text{sat},\text{stars}}/M_{\text{host},\text{disk}}$ ratio to account for the fact that the satellite particles have smaller masses.

3.4.2.1 Vertical structure of the remnants Fig. 9 shows the vertical luminosity distributions of the remnant systems for all our experiments. These have been obtained

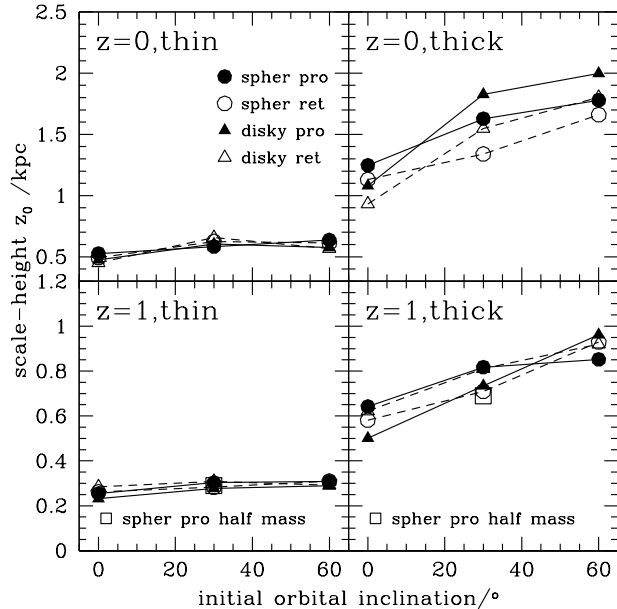


Figure 10. Scale-heights of the final systems decomposed into a “thin” and a “thick” disk. Solid/dashed lines connect prograde/retrograde satellites.

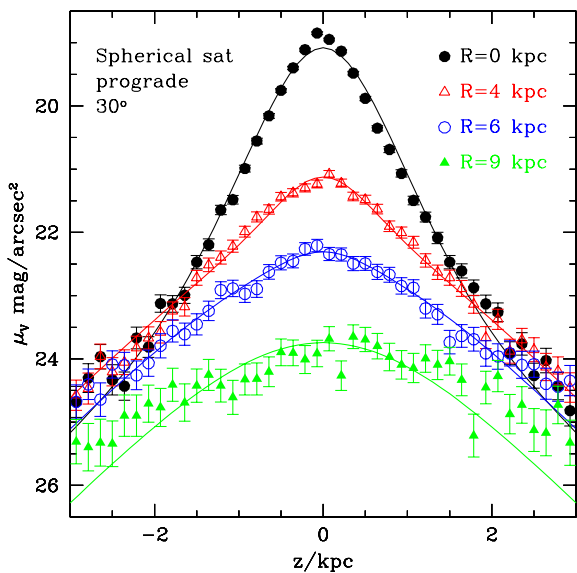


Figure 11. Surface brightness profiles as a function of height at several projected radii for one of the “ $z=1$ ” experiments. The thin remnant dominates the surface brightness in the central regions, while the thicker component is more dominant at the outskirts. Solid lines show the two-component fits at each radius.

by including all stars at all radii within $|z| < 3$ kpc for “ $z=1$ ”, and within $|z| < 5$ kpc for “ $z=0$ ”. The dotted lines correspond to a single-component sech^2 fit to the vertical profile. This figure shows that such a model clearly underestimates the luminosity at large distances from the plane, highlighting the need for a two-component decomposition.

Therefore, we fit the surface brightness as:

$$L(R, z) = \sum_{i=1}^2 L_{0,i}(R) \text{sech}^2 \left(\frac{z}{2z_{0,i}} \right) \quad (5)$$

where $z_{0,i}$ is a (luminosity weighted) exponential scale-height and $L_{0,i}$ is the central luminosity (on the midplane) of each component ($i = 1, 2$). As usual, $\mu(R, z) = 26.4 - 2.5 \log[L(R, z)]$. To compute the luminosity-weighted scale-heights we proceed as follows. First we fit independently the vertical brightness profiles in 1 kpc radial bins (within projected radii $R < 20$ kpc for “ $z=0$ ”, and $R < 10$ kpc for “ $z=1$ ”) using two components. For each radial bin we allow the algorithm to find the best central luminosities and exponential scale-heights using a Levenberg-Marquardt least-squares minimisation. The luminosity-weighted scale-height of each component is then the mean scale-height averaged over all radii and weighted by luminosity.

The fits obtained in this way are shown in Fig. 9 as solid curves. Clearly the vertical structure of our remnants is considerably better modeled by considering two disk components with different scale-heights and central surface brightness. In all cases, a thin disk is present after the merger with the satellite.

Fig. 10 shows the luminosity-weighted scale-heights of each component of the remnant systems for all our experiments. Note that the thinner component has in all cases, a very similar (and only slightly larger) scale-height to that of the initial host disk. The scale-height of thicker component is clearly larger for encounters with higher orbital inclinations. This is because there is a significantly larger vertical kinetic energy associated to the satellites’ orbital motion transferred to the disk. Spherical and disky satellite do not induce very different vertical heating on the disks. Note that less massive satellites produce final thick disks that are thinner.

Fig. 11 shows surface brightness profiles as a function of height at several projected radii for one of the experiments. Two-component fits using the luminosity-weighted scale-heights described above are also included. This figure shows that the remnant thin disk dominates the surface brightness at small radii. Note that at large radii ($R = 9$ kpc, or $\mu \sim \mu_0 + 6$) there is an indication that the thick disk is flared, and no longer follows an exponential distribution with a constant scale-height at all radii. Such flared disks have already been observed in previous studies (e.g. QG86), suggesting that flaring is a rather generic characteristic of disks heated by mergers (see Kazantzidis et al. 2007, for a derivation of how the scale-height varies with radius due to minor mergers).

3.4.2.2 Radial structure of the remnants

Figures 12 and 13 show the mass surface densities of the simulated thick disks as a function of radius, for the “ $z=0$ ” and “ $z=1$ ” configurations, respectively. Each panel is for a different inclination or different type of satellite (spherical, disky or half-mass) on prograde (red) and retrograde orbits (blue). The control disk galaxies are also shown at the initial (dotted curves) and final times (dashed curves) to calibrate the effect of the mergers against the intrinsic evolution of the host (which in all cases is negligible). In order to estimate the contribution of the satellite stars, the mass surface den-

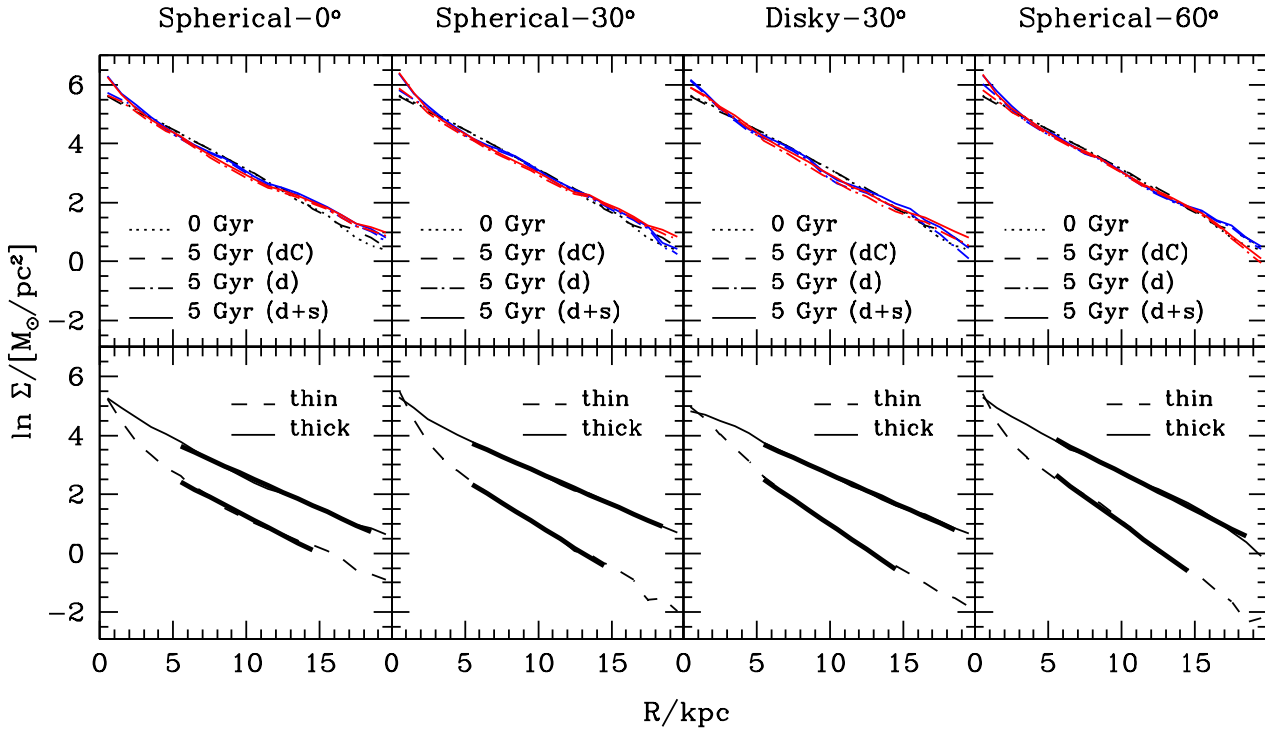


Figure 12. *Upper panels:* surface density profiles of final thick disks as a function of cylindrical radius for “ $z=0$ ”, including stars within $|z| < 5$ kpc. Red and blue lines correspond to prograde and retrograde orbits, respectively. The measurements include stars of both disk and satellite (solid) or only stars from the disk (dashed-dot). As reference, both initial (dotted) and final states (dashed) of the disk in the control model are also shown. *Lower panels:* Surface density profiles of regions dominated by thin (dashed; defined by $|z| < 0.5z_{0,thin}$) and thick (solid; $1z_{0,thin} < |z| < 5$ kpc) remnants, including the section used to compute the scale-lengths (heavy solid).

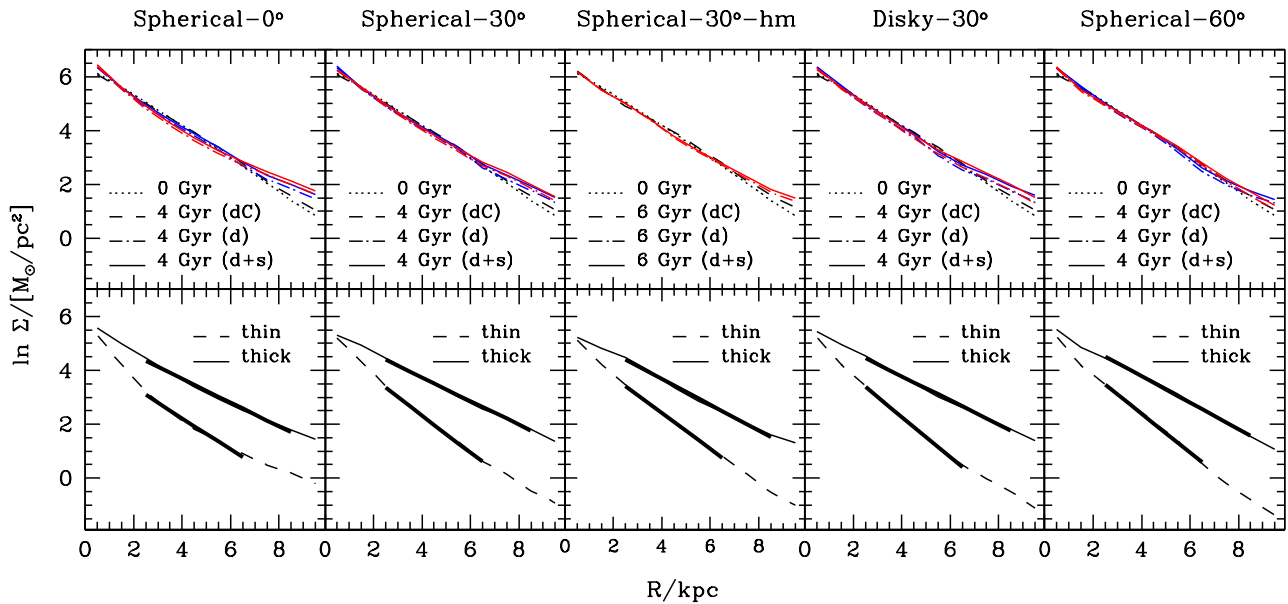


Figure 13. Same as Fig. 12 but now for the “ $z=1$ ” experiments, including stars within $|z| < 3$ kpc in the upper panels. In this case the region dominated by thick remnants is defined as $1z_{0,thin} < |z| < 3$ kpc. The column “hm” corresponds to the lighter satellite (with half the mass).

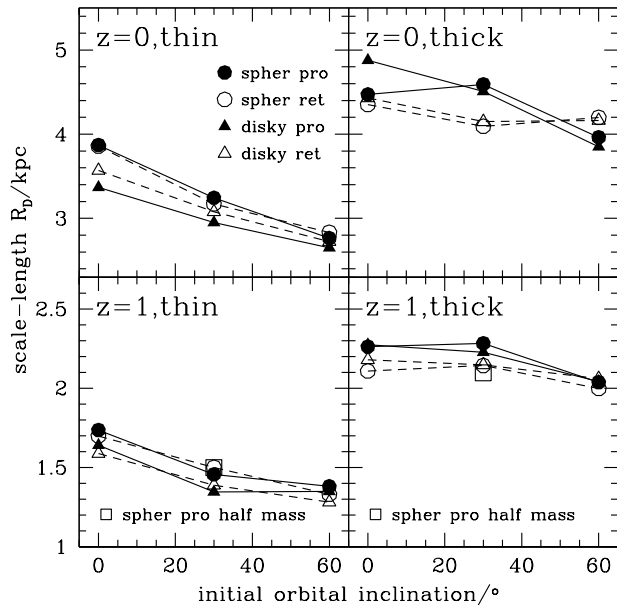


Figure 14. Scale-lengths of the remnant system for all experiments. They are obtained by decomposing the final disks into thin and thick components. Solid/dashed lines connect prograde/retrograde satellites.

sities of only host disks are plotted separately (dash-dotted curves).

For both “ $z=0$ ” and “ $z=1$ ” experiments, the surface density profiles show a mild dependence on orbital inclination (upper panels), having slightly higher surface brightness in the outskirts for lower inclinations. This tendency is mostly due to the host disk material that is transported radially outwards during the merger by transfer of energy and angular momentum.

As expected, the lighter spherical satellite (in the “ $z=1$ ” experiment) produces a smaller variation in the surface density at larger radius. In general the contribution of satellite particles to the spatial structure of final thick disks is very small. This is true at all radii except at the centre where the very dense spherical satellites accreted in the “ $z=0$ ” experiment are not completely disrupted, retaining a core and giving rise to a small “bulge-like” component (see also Fig. 3). The surface density profile does not show any strong dependence on orbit direction.

The lower panels of Figs. 12 and 13 show the surface density profiles of regions dominated either by the thin or thick remnants (for prograde experiments only) according to the decomposition performed in §3.4.2.1. These regions are defined as $|z| < 0.5z_{0,thin}$ for the thinner component, and for the thicker one from $1z_{0,thin}$ upto 5 kpc for the “ $z=0$ ” case (and upto 3 kpc for “ $z=1$ ”). The scale-lengths of each component are computed by applying a linear fit to $\ln\Sigma(R)$, avoiding non-axisymmetries associated to both the central regions and the very outskirts. Note that the linear fits consider a more extended region for thick remnants. This is to account for the dominance of thick remnants at larger radii (see Fig. 11).

Fig. 14 shows the final scale-lengths of the thick disks

as a function of the initial orbital inclinations of the satellites. In all cases, the remnant thin disks have smaller scale-lengths than their thicker counterparts, and comparable to the initial values. Low inclination encounters induce larger thick-disk scale-lengths in comparison to higher inclinations. This is because in the former cases, the orbital energy of the satellite is deposited mostly into radial motions of the stars in the disk. Similar trends are observed for the galaxies in Yoachim & Dalcanton (2006). However, this should be taken with great care because our comparison is to the remnant thin disk and not to the present-day thin disk of those galaxies (because we do not model this). Furthermore we have not modeled the response of the remnant thin or thick disks to the formation of the new thin disk.

We compute the total mass associated to each of disk component using the fits just derived. We find that the total mass associated to the remnant thin disk is $\sim 15\%$ – 25% of the total stellar mass of the system for both “ $z=0$ ” and “ $z=1$ ” experiments.

In general, the presence of a thin remnant after the merger is in agreement with results by Kazantzidis et al. (2007), although the total mass associated to this component is significantly smaller in our case ($< 25\%$ versus $\sim 80\%$). This is maybe due to the fact that Kazantzidis et al. (2007) do not follow the full merger event, but only let their satellites have one passage around their host disk, hence perhaps increasing its chances of remaining relatively cold. Note however, that in their work this bombardment is repeated in a sequence using six different satellites.

3.4.2.3 Distribution of satellite vs host disk stars

Fig. 15 shows the final relative number $N_s/(N_s + N_d)$ of stellar satellite particles as a function of radius in the resulting thick disks for mergers configured at “ $z=0$ ” and “ $z=1$ ”. Recall that the number of satellite particles has been renormalised according to $N_s = N_{sat,stars} \times M_{sat,stars}/M_{disk}$.

As mentioned before, in the “ $z=0$ ” experiments, spherical satellites have a higher mean density than the host disk. This causes the core to reach the host disk centre almost intact, representing $\sim 50\%$ of the total number of particles near the centre of the final thick disk. In comparison, this ratio drops to 5% for the disky satellites. At both intermediate and larger radii the fraction of particles from the spherical satellites is roughly constant, independently of either orbital inclination or sense of rotation. On the other hand disky satellites are disrupted at large radii, where their debris is deposited. Furthermore, the lower the inclination, the higher the fraction at a given radius, as naturally expected.

For “ $z=1$ ” both spherical and disky satellites are completely destroyed. The relative fraction of satellite stars increases with radius and, as expected, at the centre the relative number of satellite particles is smaller for the lighter satellite. The observed trend with orbital inclination in spherical and disky satellites at “ $z=0$ ” is confirmed for the “ $z=1$ ” configuration.

Fig. 16 shows the fraction of satellite particles plotted now as a function of the vertical direction at a radius $R=4.5$ kpc, for spherical and disky satellites in the “ $z=1$ ” experiments. The radius corresponds to 2.4 initial scale-lengths in this experiment. In this figure the distances from the plane are normalised by the scale-height obtained by fitting locally a single *sech*² law to the vertical density distribution.

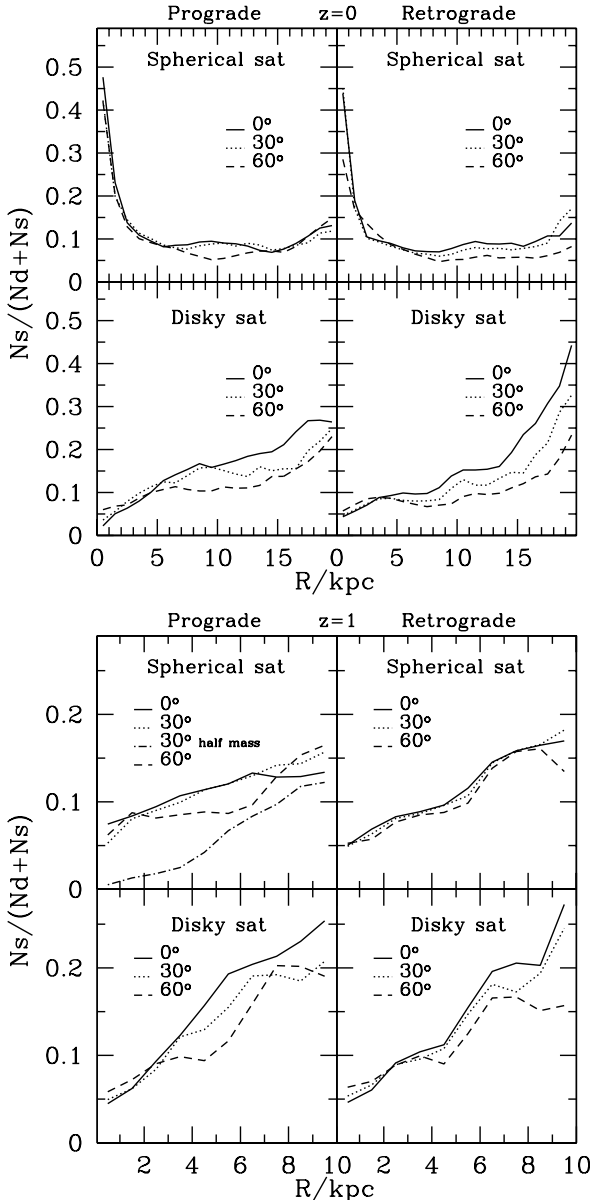


Figure 15. Relative number of satellite particles in the final systems as a function of cylindrical radius for the “ $z=0$ ” (top) and “ $z=1$ ” (bottom) experiments.

Therefore Z_0 it is close to a luminosity weighted average of the scale-heights of the thin and thick disks given in Fig. 10. This figure shows that the fraction of accreted particles as a function of distance from the plane, when normalised by this scale-height, *only* depends on the mass ratio between the satellite and host. E.g., at $z = 4Z_0$ the fraction of particles reflects the mass ratio of the merger. The same behaviour is observed in the “ $z=0$ ” experiments.

3.4.3 Kinematical Properties

The structural decomposition made in §3.4.2.1 should also be reflected in the kinematics of the stars in our systems in order to be physically meaningful. Fig. 17 shows this is in-

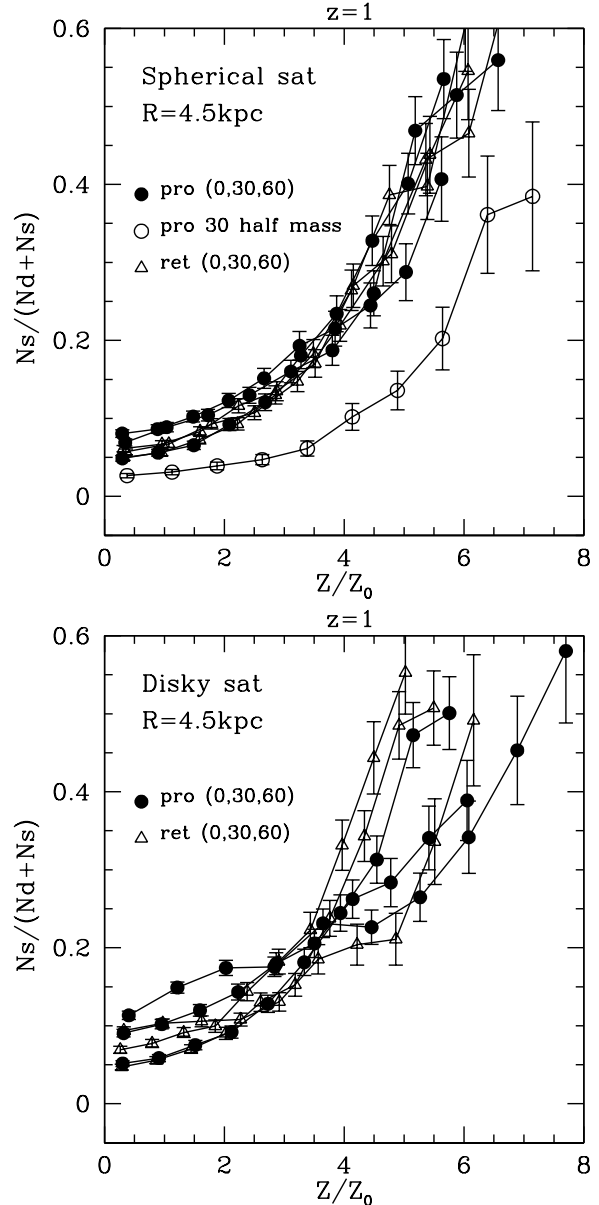


Figure 16. Relative number of satellite particles for our “ $z=1$ ” experiments, as a function of distance from the disk plane. Distances from the plane are normalised by the respective scale-height at a distance of $R = 4.5$ kpc (i.e. 2.4 scale-lengths of the original disk). Note that the scale-height here is obtained by fitting locally a single $sech^2$ law to the vertical density distribution, and hence it is close to a luminosity weighted average of the scale-heights of the thin and thick disk shown in Figure 10.

deed the case. Here we plot the z -velocity distribution within a spherical volume of 1 kpc radius centred at $R \sim 4$ kpc on the midplane for one of our experiments (“ $z=1$ ”, spherical satellite, prograde, 30°). The dashed curve shows that a single Gaussian (corresponding to a one-component system) misses the peak of the distribution highlighting the need for a second (colder) component. We therefore proceed to fit all velocity distributions (also the radial and azimuthal) with two Gaussians. We constrain the relative normalisation of these by using the photometric decomposition from

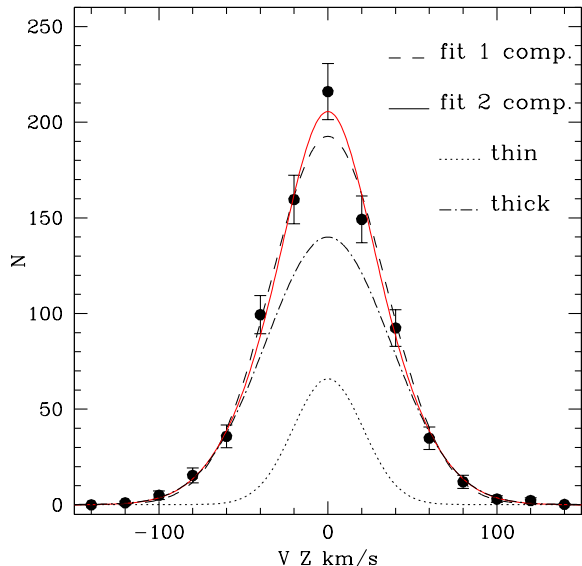


Figure 17. Example of decomposition of the vertical velocity distribution into a cold component (associated to the remnant thin disk) and a hot one (the thick disk). The normalisation of each component has been fixed according to the photometric decomposition of §3.4.2.1 (see text). The contribution of the two components is separately shown.

§3.4.2.1, which determines the relative number of stars from each component within a given volume. The solid curve in Fig. 17 is an example of the quality of the fit obtained in this way, whose reduced- χ^2 ($= 0.47$) is lower than that obtained for a single Gaussian ($= 0.68$).

The transformation of orbital energy into thermal energy (random motions) in the disk is evident in Figs. 18 and 19. Here we show the radial, azimuthal and vertical velocity dispersions along with the mean rotational velocities of the thick disks present in our systems as a function of cylindrical radius. These quantities have been computed at each cylindrical radius in concentric rings of 1 kpc width, including stars between $|z| < 3$ kpc, for “ $z=0$ ”, and $|z| < 1.5$ kpc, for “ $z=1$ ” experiments.

In all our experiments, the vertical and azimuthal velocity dispersions of the remnant thin disks are very similar to those of the initial host disk, and hence are not plotted for clarity. On the other hand, the radial velocity dispersions are generally larger by 5 – 10 km/s at all radii.

Figures 18 and 19 show that the radial σ_R and azimuthal σ_ϕ velocity dispersions of the thicker component are larger for lower inclination orbits moving in the prograde sense. The opposite trend is observed for the vertical velocity dispersion σ_z . This is as expected given our previous discussion on the evolution of the scale-heights and scale-lengths and their dependence on orbital inclination. Spherical and disk satellites give rise to similar velocity distributions.

The resulting velocity dispersions σ_R and σ_z for retrograde orbits are similar to the prograde cases. On the other hand, the azimuthal velocity distributions of the heated disk stars generally require an additional component to account for the contribution of the (accreted) counter-rotating stars (Villalobos & Helmi, in prep). The global velocity disper-

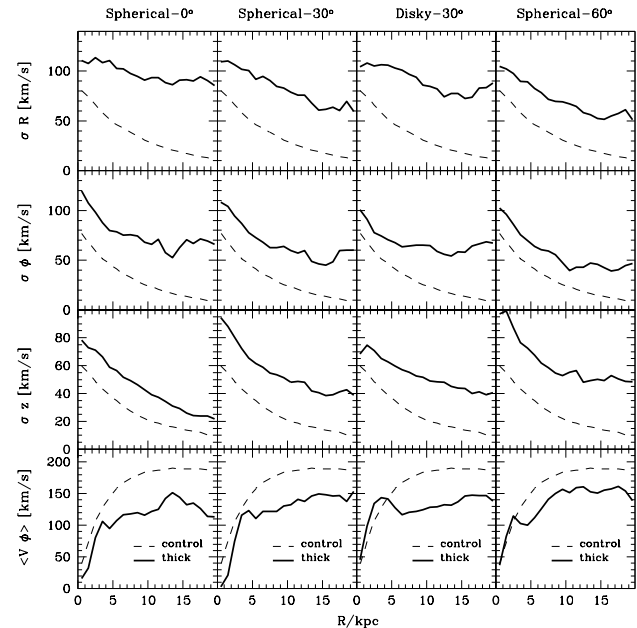


Figure 18. Final dynamical properties of the thick disk components for our prograde “ $z=0$ ” experiments. These properties have been computed at $t = 5$ Gyr for stars within $|z| < 3$ kpc in concentric rings of 1 kpc width, using the decomposition described in §3.4.2.1. As reference, the final state of the disk in the control model is also shown (dashed).

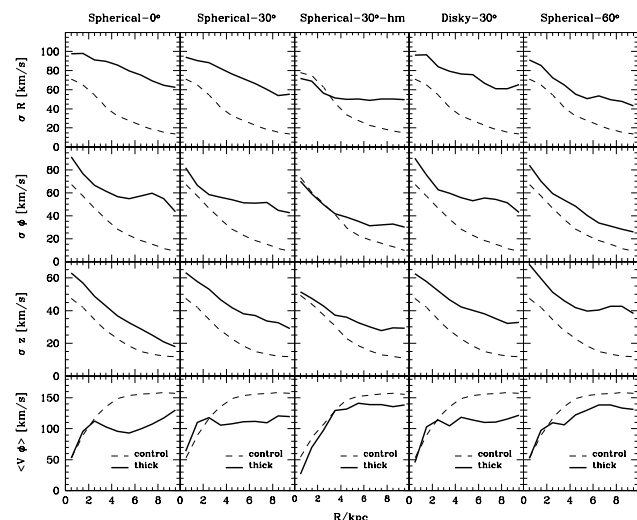


Figure 19. Final dynamical properties of thick disk components for our prograde “ $z=1$ ” experiments. The column “hm” show the satellite with half the mass. As in the previous figure, the properties have been computed within concentric rings of 1 kpc width, now for particles with $|z| < 1.5$ kpc at $t = 4$ Gyr (except for the “hm” satellite, where $t = 6$ Gyr). The final state of the disk in the control model is shown by the dashed curves.

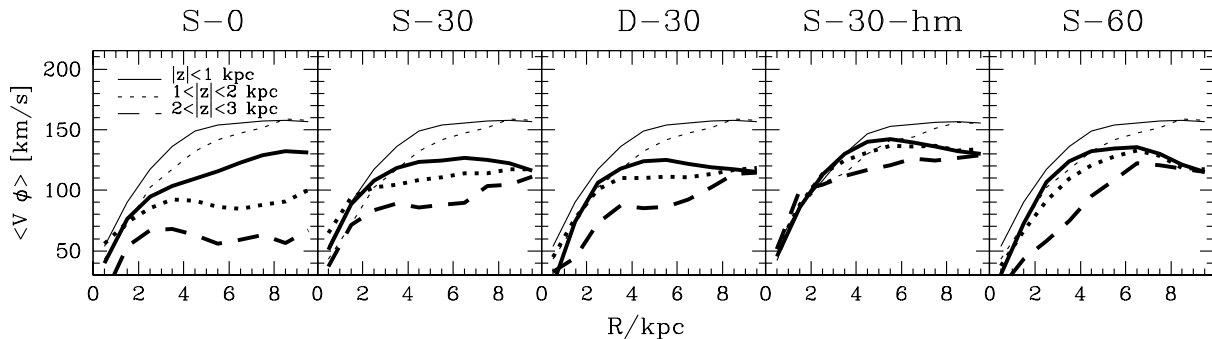


Figure 20. Mean azimuthal velocities of the “stars” in our experiments at several heights above the plane as a function of radius for our “ $z=1$ ” experiments in prograde orbits. Thick lines include particles from both the heated disk and satellite, while the thin lines correspond to the disk in the control model (the highest z -range is not shown in this case because there are too few disk particles at that distance from the midplane). The same behaviour is observed in our “ $z=0$ ” experiments (not shown).

sion (that would be obtained by imposing a single Gaussian for the thick component) would be in this case significantly larger at large radii for retrograde orbits, except for those with high inclination.

In general, the mean rotational velocities $\overline{v_\phi}$ of the thick disks differ noticeably from the coeval control simulation in all cases, by dropping ~ 60 km/s although with a mild dependence on the orbital inclination. Low inclination encounters produce thick disks that rotate slower, implying larger asymmetric drifts. This is also evidenced by their larger radial and azimuthal velocity dispersions, as discussed above. The mean rotational velocity of thick disks which are the result of encounters with satellites on counter-rotating orbits is lower due to the contribution of the accreted stars, particularly at large radii.

The mean rotational velocity also shows noticeable differences with inclination when it is measured away from the midplane of the thick disk. In Fig. 20 we plot $\overline{v_\phi}$ for the prograde experiments at different heights above the plane, without making a distinction between the thin and thick disk components. Note that for $|z| > 1$ kpc we are really measuring the kinematics of the thick disk component since the contribution of the remnant thin disk is negligible. Satellites with lower initial orbital inclinations induce a rotational lag, whose magnitude increases with height above the plane. This is because such satellites are more efficient in heating the disk radially at every height, leading to a larger asymmetric drift.

In Fig. 21 we plot the ratio σ_Z/σ_R of the thick disk component as a function of radius for different prograde experiments. Recall that the initial (and the control) disk has a (nearly) constant $\sigma_Z/\sigma_R \sim 0.7$. This figure clearly shows that σ_Z/σ_R can be used as a discriminant of the initial inclination of the satellite. The reason for this strong dependence on inclination is essentially due the fact that a satellite on a highly inclined orbit will induce a much larger change in σ_Z at large radii than one on a co-planar orbit.

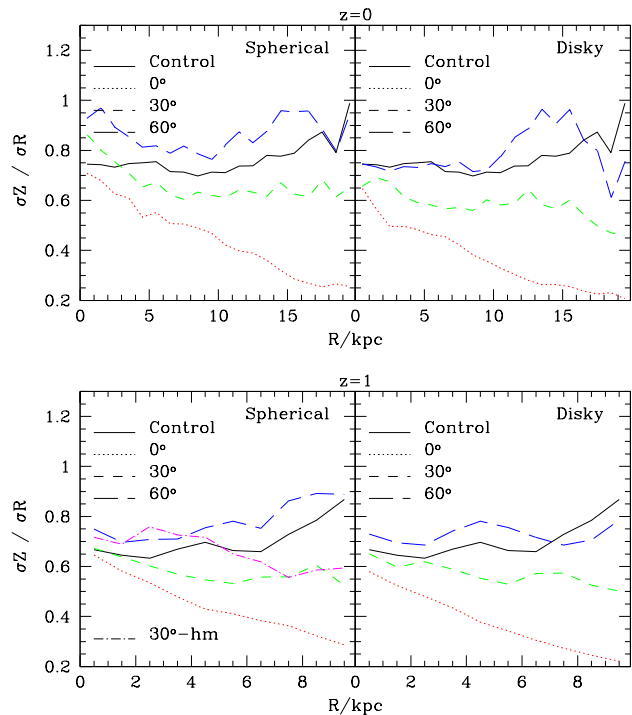


Figure 21. Final σ_Z/σ_R of thick remnants as a function of distance on the plane for different initial stellar distributions and orbital inclinations of the satellites. The control disks have a steady $\sigma_Z/\sigma_R \sim 0.7$. Only prograde orbits are shown.

4 DISCUSSION

Previous works investigating the response of a host disk galaxy to one or more infalling satellites provide us with a valuable description of the dynamical effects involved in the process (QG86; Tóth & Ostriker 1992; QHF93; WMH96; HC97; VW99; Benson et al. 2004). HC97 find that a massive satellite (30% of M_{disk}), as it decays due to dynamical friction, can tilt the orientation of the disk up to 10° and cause warping. These effects illustrate the strong transfer of angu-

lar momentum from the infalling satellite to the host disk. VW99 note that satellites in prograde orbits mostly increase the disk heating. On the other hand retrograde orbits are more efficient in tilting the disk orientation. Benson et al. (2004) show that more massive and more concentrated satellites increase the difference between the amount of disk heating caused by prograde and retrograde orbits. QG86 indicate that most of the kinetic energy of the infalling satellite is deposited on the plane of the disk and a small quantity heats up the vertical motions of disk particles. This shows that velocity dispersions in the host disk are not increased isotropically by the satellite. QHF93 note that most of the heating on the plane of the disk is caused by spiral arms stimulated by the decaying satellite. These arms also transfer angular momentum radially outwards, expanding the disk. QG86 and QHF93 also show that the vertical structure of the disk is not uniform across the disk. Instead, the scale-height of the host disks increases at larger radii. Our simulations are able to confirm most of the aforementioned dynamical effects but also show a significantly larger tilting than previously found, both for the prograde and retrograde cases. This can be traced back to the fact that in our experiments, the accreted satellite is initially much more massive and is launched from a significantly larger distance (see §3.3).

4.1 Choice of massive satellites to heat disks up

Cosmological simulations show that massive mergers like those in our “z=1” experiments are likely to have happened during the life-time of a Milky Way-sized host system. For instance, Kazantzidis et al. (2007) estimate the number of massive subhalos accreted since $z \sim 1$ as at least one object with a mass $\sim M_{disk}$ and five objects more massive than 20% M_{disk} . This is consistent with simulations by other groups (e.g. Stoehr 2006; De Lucia & Helmi 2008), and supported by the detailed study by Stewart et al. (2007). Even though massive mergers may be less frequent they are able to reach the centre of the host system thanks to dynamical friction, causing important changes in the structure and kinematics of the host disk. In principle, this could imply that a Milky Way-like disk would experience only one severe change of orientation since $z \sim 1$ and also that only one massive satellite would be needed to heat up a pre-existing disk to give rise to a thick disk.

4.2 Observations of thick disks

Pohlen et al. (2004) have carried out photometric thick/thin disk decompositions and characterised properties such as scale-length and scale-height for a sample of eight S0 edge-on galaxies by fitting 3D disk models. The authors find that the mean scale-height of the thick disk is between 2.4 and 5.3 times larger than that of the thin disk; while the mean scale-length is about twice, ranging from 1.6 to 2.6. In general these values are consistent the results obtained by other authors for S0, Sab, Sb, Sbc, Scd and Sd galaxies (e.g., van der Kruit 1984; de Grijs & van der Kruit 1996; de Grijs & Peletier 1997; Pohlen et al. 2004; Yoachim & Dalcanton 2006), including the Milky Way (Ojha 2001; Larsen & Humphreys 2003). If we assume that the structure of our simulated disks are not

strongly affected by the formation of a new thin disk, and that these new thin disks will follow the same distribution as the remnant thin disks in our models, we can take the ratio of scale-heights obtained for our experiments at the final time at face value. Typically there is an increase in the scale-height by a factor 3 – 6, while the scale-lengths are only slightly larger (with final-to-initial ratios between 1 and 1.4). These values appear to be in agreement with the range of ratios observed in general in spiral galaxies. However, this should be taken with great care because of the strong assumptions just made.

Most of our thick disks are significantly flared in the outer regions. This has also been found in other studies (e.g. Kazantzidis et al. 2007; Read et al. 2008), with varying strengths, depending on the initial configuration of the system. For example, galaxies with a bulge or embedded in a cored dark-matter halo are more stable, and suffer from less flaring (Naab & Burkert 2003; Bournaud et al. 2005; Kazantzidis et al. 2007). This implies that we might expect to find in nature thick disks with varying degrees of flaring. However, quantifying this requires reaching extremely low surface brightness levels, approximately 6 – 7 magnitudes below the peak brightness of the *thick* disk. This is very challenging and has not yet been achieved in studies of surface photometry, which typically reach about 5 magnitudes below the peak value of the *thin + thick* disks. For example, Neeser et al (2002) detected a thick disk in a low-surface brightness galaxy. They reach a surface brightness level in the R-band of 29 mag/arcsec². This is almost 7 magnitudes below the central thin + thick disk value, and a very marginal indication of a flare is apparent on the east side of the thick disk at a distance of ~ 3 scale-lengths. Morrison et al. (1997) in their study of NGC891 (a late type disk with a small bulge) do not find evidence for flaring in the thick disk, but “only” reach down to 26 mag/arcsec² in R, which is about 6 magnitudes below the central surface brightness of the dominant disk component.

Dalcanton & Bernstein (2002) have found a vertical colour-gradient in their sample of galaxies, in the sense that the thick disks are redder, and consistent with a relatively old (> 6 Gyr) stellar population. In the scenario we envisage for the formation of thick disks we would expect two sources of color-gradients. The first would be due to the transition from the population of young thin disk stars to the thick disk stars formed in situ, i.e. originating from a pre-existing thin disk. Unfortunately, because we do not model the formation of a new disk from freshly accreted gas, we cannot make a quantitative comparison. The second source of a change in stellar populations would be due to the difference between accreted satellite stars and those formed in situ in the (heated) disk. Our Figures 15 and 16 show that the fraction of satellite particles is generally quite low. Only at distances above the plane of approximately 6 thick disk scale-heights, the number of accreted stars is comparable to that of the heated disk. This implies that this second gradient should be weaker, and is unlikely to be detected in current observations because at these heights, the typical surface brightness levels are exceedingly low (see Figure 11).

Kinematically, the values of the velocity ellipsoids of our thick disks, measured at $R \approx 2.4R_D$, are in good agreement with the one observed at the solar radius in the Milky Way ($\sigma_R, \sigma_\phi, \sigma_z \sim (65, 54, 38)$ km/s (e.g., see

Layden et al. 1996; Chiba & Beers 2001; Soubiran et al. 2003; Alcobé & Cubarsi 2005; Vallenari et al. 2006; Veltz et al. 2008). The values of σ_Z/σ_R measured by most of these authors are typically $\sim 0.6^4$, suggesting that the thick disk of the Galaxy could have been produced by a merger of intermediate inclination (see Fig. 21). The differences between the mean rotational velocity of the final thick disk and that of the remnant thin disk are $\Delta\bar{v}_\phi \sim 40\text{--}50$ km/s. Note that these values cannot be interpreted directly as the observed rotational lag between the thin and thick disks in the Milky Way since we do not include gas in our simulations that later on can collapse and actually form a new thin disk (see §4.4.1).

4.3 Our simulations in the context of M31

It is important to notice that in our experiments configured at “z=0” the initial properties of the host disk, before the merger with the satellite, resemble the properties of the current thin disk of the Galaxy. This implies that the final thick disks generated in our experiments are too massive and do not represent direct analogues of the thick disk of the Milky Way. However this set of simulations may be useful for understanding the evolution of M31, which is likely to have experienced recent merger events as may be inferred from the rich and complex structures present in its outskirts (Ibata et al. 2007, and references therein).

For example, Ibata et al. (2005) discovered an extended and clumpy disk-like structure around M31 with a scale-length similar to that of the main disk, rotating ~ 40 km/s slower and with a rather low velocity dispersion of ~ 30 km/s. Its stellar population has homogeneous kinematics and abundances over the entire region where it is observed, which suggests that it was formed in a single global event. However, it is not straightforward to link the extended disk of M31 to the thick disk modeled here, mainly because of the much higher velocity dispersions of the final thick disks in our simulations.

The giant stream of M31, thought to originate in the disruption of a satellite with mass $\sim 10^9 M_\odot$, and the so-called eastern and western “shells” (Ibata et al. 2007), may be related given the similarities of their stellar populations. In the context of our simulations, this would be quite natural. Analogous structures are observed as the satellite is disrupted as shown in Figs. 5 and 6 for prograde orbits in face-on view at 1.5 Gyr (see also Fardal et al. 2007; Mori & Rich 2008). It is interesting to note that much sharper and longer lasting shells are generated by disk satellites compared to spherical ones.

4.4 Caveats

4.4.1 Lack of gas physics in our simulations

In this paper we have focused on the collisionless interactions between a disk galaxy and a satellite, with both dark matter and stellar components, without including gas physics

nor star formation which may affect the interactions and the final thick disk’s properties. This is potentially the most crucial simplifying assumption in this study since disk galaxies were presumably much more gas rich at high redshift (Robertson et al. 2006).

The lack of gas physics implies that the modeled disks do not grow in stellar mass or in size during the timespan of the merger (except of course through the dynamical heating processes described above). Furthermore, it is likely that such mergers would trigger a (strong) burst of star formation. These new stars would be relatively old at the present day and located in a thinner structure. On the other hand, some orbital energy deposited by the infalling satellite into the gas could be radiated away from the system, reducing the dynamical damage done to the disk (QHF93). For example, in recent work Hopkins et al. (2008) based on Younger et al. (2008) suggested that the change in the structural parameters depends on the fraction of gas f_g available as $\delta H \sim (1 - f_g)\delta H_*$, where δH_* corresponds to the scale change in the purely dissipationless case.

Any remaining (and presumably heated) gas would eventually cool and settle down to form a new thin disk. This slow accumulation of gas on the midplane should induce a contraction of the thick disk. For example, Elmegreen & Elmegreen (2006) estimate that this contraction leads to a decrease in the scale-height of the contracted thick by $\sim 40\%$ and an increase of the velocity dispersion by $\sim 50\%$. Furthermore, the accretion of fresh gas from the inter-galactic medium is likely to also be important, and will lead to further changes to the properties of the merger products studied here.

4.4.2 Time-dependence of gravitational potential

In general, the structure of a dark matter halo evolves with time through mergers and slow accretion. However, in our simulations we have neglected any cosmological evolution of the structure of the host halo during and after the merger with the satellite. This simplification may be justified by recent studies (e.g., Wechsler et al. 2002; Romano-Diaz et al. 2006), which have shown that the structure of dark halos is very stable within the scale radius r_s after the phase of active mergers, which for a disk galaxy must have ended at redshifts $\sim 0.5 - 1$. This is indeed the region that we follow dynamically in our simulations, after the initial decay of the satellite due to dynamical friction, which lasts typically less than 1 Gyr. Therefore, the final thick disks are well within this scale radius, being $r_s \sim 6$ and ~ 11 times the final scale-lengths in the “z=0” and “z=1” experiments, respectively.

5 SUMMARY AND CONCLUSIONS

We have performed numerical simulations of the heating of a disk galaxy by a single relatively massive merger. These mergers lead to the formation of thick disks whose characteristics are similar, both in morphology as in kinematics, to those observed in the Milky Way and other spiral galaxies.

The simulations explore several configurations of the progenitor systems whose properties have been scaled at two different redshifts in order to study the formation of thick

⁴ Although Veltz et al find $\sigma_Z/\sigma_R \sim 0.9$, which could be due to the fact that the assumption of isothermality for the velocity distribution is not valid.

disks at different epochs. The satellites have total masses of 10% and 20% that of the host galaxy and have been modeled self-consistently as a stellar component immersed in a dark matter halo. The stellar components have either a spherical or disky distribution. The satellites have been released far away from the host disk, with initial orbital parameters that are consistent with cosmological studies. Additionally, three different initial orbital inclinations of the satellites have been studied in both prograde and retrograde directions with respect to the rotation of the host disk.

We find that as the satellite galaxies spiral in through dynamical friction, significant asymmetries are visible, both in the host disk and in the satellite debris. Particularly interesting are the low surface brightness shells, especially visible in the outskirts of the final thick disks, that last for about 1.5 to 2 Gyr after the merger has been completed. These shells acquire relevance in the case of Andromeda where according to recent studies a couple of these features are likely associated to the event that also gave rise to the giant stream (Ibata et al. 2007, and references therein).

Despite the relatively large mass ratios, the infalling satellites do not fully destroy the host disk, but merely heat it and tilt it. The host disks are found to change their orientation both for the prograde and retrograde encounters. Furthermore, a remnant thin component containing between 15 and 25 per cent of the total stellar mass of the system is present at the final time in all our experiments. This prediction of the minor merger model might be potentially relevant to understand the presence of a very old thin disk in the Milky Way.

The scale-lengths of the final thick disks are slightly more extended than those of the original host disk while the scale-heights are between three and six times larger, depending on the initial inclination of the satellite. The scale-heights have also increased in proportion to the inclination of the encounter, and the outer disks are noticeably flared. If this is the case for the thick disk of the Milky Way, part of the flared material could be (confused with) the Monoceros ring.

In our simulations, the outer isophotes of the final thick disks (measured at surface brightness levels >6 mag below the central value) are consistently more boxy than the inner ones. The eventual detection of such degree of boxiness, especially for bulgeless galaxies, would provide support for a formation process as that modeled here.

Interestingly, the fraction of satellite particles at a given galactic radius as a function of height above the plane, when normalised by the (luminosity-weighted) scale-height, *only* depends on the mass ratio between the satellite and host and not on stellar morphology of the satellite or type of orbit. For instance, at a distance of 4 scale-heights the fraction of satellite particles reflects the mass ratio of the merger.

We find that satellite stars do not dominate the luminosity of the thick disk until rather far above the midplane. In this sense, the existence of a counter-rotating thick disk, detected by Yoachim & Dalcanton (2005) only ~ 2 thick-disk scale-heights above the midplane, can only be explained in the context of our models if the (young) thin disk formed from freshly accreted counter-rotating gas. The remaining possibility is, of course, that the thick disk formed exclusively by direct accretion of stars from an infalling satellite. Relatively fast rotating thick disks (like the one of the Milky

Way) may be more easily explained by disk heating formation, since a random distribution of accreted satellites would seem to have less chance of producing thick disks with strong coherent rotation.

If taken at face value the velocity ellipsoids of the simulated thick disks are in good agreement with observations of the Galactic thick disk at the solar radius. The rotational lag may also be consistent with observations. These statements are however only valid if we neglect further significant evolution due to the formation of a thin disk component from freshly accreted gas. The observed trend of the ratio σ_Z/σ_R with radius in the final thick disks is found to be a very good discriminant of the initial inclination of the decaying satellite. In the case of the Milky Way, the observed σ_Z/σ_R at the position of the Sun is ~ 0.6 (e.g., Chiba & Beers 2001; Vallenari et al. 2006), suggesting that the thick disk of the Galaxy could have been produced by a merger of intermediate inclination. Measurements of the mean rotational velocity in the final thick disks, at several heights from the midplane, indicate that satellites with lower initial inclinations are more efficient in introducing asymmetric drifts dependent on height. This implies that the possible existence of vertical gradients in the mean rotational velocity in the thick disk of the Galaxy (Girard et al. 2006) would also favour mergers with either low or intermediate orbital inclination. We defer to paper II a more detailed analysis of the phase-space structure of the merger product. We expect this will lead to new constraints on the mechanism described here for the formation of the Galactic thick disk.

ACKNOWLEDGEMENTS

We are grateful to the referee for the extensive and very insightful comments which have led to a number of significant improvements in our manuscript. We thank M. C. Smith and L. Sales for stimulating discussions and suggestions, and S. C. Trager and R. Sanders for useful remarks. We acknowledge financial support from the Netherlands Organisation for Scientific Research (NWO). The simulations were run in the Linux cluster at the Centre for High Performance Computing and Visualisation (HPC/V) of the University of Groningen in The Netherlands.

REFERENCES

- Abadi M. G., Navarro J. F., Steinmetz M., Eke V. R., 2003, *ApJ*, 597, 21
- Aguerri J. A. L., Balcells M., Peletier R. F., 2001, *A&A*, 367, 428
- Alcobé S., Cubarsi R., 2005, *A&A*, 442, 929
- Ardi E., Tsuchiya T., Burkert A., 2003, *ApJ*, 596, 204
- Athanassoula E., Fady E., Lambert J. C., Bosma A., 2000, *MNRAS*, 314, 475
- Athanassoula E., Lambert J. C., Dehnen W., 2005, *MNRAS*, 363, 496
- Bekki K., Chiba M., 2001, *ApJ*, 558, 666
- Bender R., Doebereiner S., Moellenhoff C., 1988, *A&AS*, 74, 385
- Benson A. J., 2005, *MNRAS*, 358, 551

- Benson A. J., Lacey C. G., Frenk C. S., Baugh C. M., Cole S., 2004, *MNRAS*, 351, 1215
- Berentzen I., Athanassoula E., Heller C. H., Fricke K. J., 2004, *MNRAS*, 347, 220
- Binney J., Tremaine S., 1987, *Galactic dynamics*. Princeton, NJ, Princeton University Press, 1987, 755 p.
- Blumenthal G. R., Faber S. M., Flores R., Primack J. R., 1986, *ApJ*, 301, 27
- Bournaud F., Elmegreen B. G., Elmegreen D. M., 2007a, *ApJ*, 670, 237
- Bournaud F., Jog C. J., Combes F., 2005, *A&A*, 437, 69
- , 2007b, *A&A*, 476, 1179
- Brook C. B., Gibson B. K., Martel H., Kawata D., 2005, *ApJ*, 630, 298
- Brook C. B., Kawata D., Gibson B. K., Freeman K. C., 2004, *ApJ*, 612, 894
- Burkert A., Truran J. W., Hensler G., 1992, *ApJ*, 391, 651
- Burstein D., 1979, *ApJ*, 234, 829
- Chen B., the SDSS Collaboration, 2001, *ApJ*, 553, 184
- Chiba M., Beers T. C., 2001, *ApJ*, 549, 325
- Cox T. J., Younger J., Hernquist L., Hopkins P. F., 2008, in *IAU Symposium*, Vol. 245, *IAU Symposium*, pp. 63–66
- Dalcanton J. J., Bernstein R. A., 2000, *AJ*, 120, 203
- , 2002, *AJ*, 124, 1328
- de Grijs R., Peletier R. F., 1997, *A&A*, 320, L21
- de Grijs R., van der Kruit P. C., 1996, *A&AS*, 117, 19
- De Lucia G., Helmi A., 2008, *ArXiv e-prints*, 804
- de Rijcke S., Michielsen D., Dejonghe H., Zeilinger W. W., Hau G. K. T., 2005, *A&A*, 438, 491
- di Matteo P., Combes F., Melchior A.-L., Semelin B., 2007, *A&A*, 468, 61
- Eggen O. J., Lynden-Bell D., Sandage A. R., 1962, *ApJ*, 136, 748
- Elmegreen B. G., Elmegreen D. M., 2006, *ApJ*, 650, 644
- Fardal M. A., Guhathakurta P., Babul A., McConnachie A. W., 2007, *MNRAS*, 380, 15
- Font A. S., Navarro J. F., Stadel J., Quinn T., 2001, *ApJ*, 563, L1
- Freeman K., Bland-Hawthorn J., 2002, *ARA&A*, 40, 487
- Fuhrmann K., 2004, *Astron. Nachr.*, 325, 3
- Gauthier J.-R., Dubinski J., Widrow L. M., 2006, *ApJ*, 653, 1180
- Gilmore G., Reid N., 1983, *MNRAS*, 202, 1025
- Gilmore G., Wyse R. F. G., 1986, *Nature*, 322, 806
- Gilmore G., Wyse R. F. G., Norris J. E., 2002, *ApJ*, 574, L39
- Girard T. M., Korchagin V. I., Casetti-Dinescu D. I., van Altena W. F., López C. E., Monet D. G., 2006, *AJ*, 132, 1768
- Hayashi H., Chiba M., 2006, *PASJ*, 58, 835
- Helmi A., Navarro J. F., Meza A., Steinmetz M., Eke V. R., 2003, *ApJ*, 592, L25
- Helmi A., Navarro J. F., Nordström B., Holmberg J., Abadi M. G., Steinmetz M., 2006, *MNRAS*, 365, 1309
- Hernquist L., 1990, *ApJ*, 356, 359
- , 1993, *ApJS*, 86, 389
- Hernquist L., Quinn P. J., 1988, *ApJ*, 331, 682
- , 1989, *ApJ*, 342, 1
- Hopkins P. F., Hernquist L., Cox T. J., Younger J. D., Besla G., 2008, *ArXiv e-prints*, 806
- Huang S., Carlberg R. G., 1997, *ApJ*, 480, 503
- Ibata R., Chapman S., Ferguson A. M. N., Lewis G., Irwin M., Tanvir N., 2005, *ApJ*, 634, 287
- Ibata R., Martin N. F., Irwin M., Chapman S., Ferguson A. M. N., Lewis G. F., McConnachie A. W., 2007, *ApJ*, 671, 1591
- Jedrzejewski R. I., 1987, *MNRAS*, 226, 747
- Jensen E. B., Thuan T. X., 1982, *ApJS*, 50, 421
- Jesseit R., Naab T., Burkert A., 2005, *MNRAS*, 360, 1185
- Kazantzidis S., Bullock J. S., Zentner A. R., Kravtsov A. V., Moustakas L. A., 2007, *ArXiv:0708.1949*, 708
- Kazantzidis S., Magorrian J., Moore B., 2004, *ApJ*, 601, 37
- Khochfar S., Burkert A., 2006, *A&A*, 445, 403
- Kregel M., van der Kruit P. C., de Grijs R., 2002, *MNRAS*, 334, 646
- Kroupa P., 2002, *MNRAS*, 330, 707
- Larsen J. A., Humphreys R. M., 2003, *AJ*, 125, 1958
- Layden A. C., Hanson R. B., Hawley S. L., Klemola A. R., Hanley C. J., 1996, *AJ*, 112, 2110
- Lewis J. R., Freeman K. C., 1989, *AJ*, 97, 139
- Martin N. F., Ibata R. A., Bellazzini M., Irwin M. J., Lewis G. F., Dehnen W., 2004, *MNRAS*, 348, 12
- Mihos J. C., Walker I. R., Hernquist L., Mendes de Oliveira C., Bolte M., 1995, *ApJ*, 447, L87+
- Mo H. J., Mao S., White S. D. M., 1998, *MNRAS*, 295, 319
- Mori M., Rich R. M., 2008, *ApJ*, 674, L77
- Morrison H. L., Miller E. D., Harding P., Stinebring D. R., Boroson T. A., 1997, *AJ*, 113, 2061
- Mould J., 2005, *AJ*, 129, 698
- Naab T., Burkert A., 2003, *ApJ*, 597, 893
- Naab T., Jesseit R., Burkert A., 2006, *MNRAS*, 372, 839
- Naab T., Trujillo I., 2006, *MNRAS*, 369, 625
- Navarro J. F., Frenk C. S., White S. D. M., 1997, *ApJ*, 490, 493
- Navarro J. F., Helmi A., Freeman K. C., 2004, *ApJ*, 601, L43
- Norris J. E., Ryan S. G., 1991, *ApJ*, 380, 403
- Ojha D. K., 2001, *MNRAS*, 322, 426
- Pardi M. C., Ferrini F., Matteucci F., 1995, *ApJ*, 444, 207
- Pohlen M., Balcells M., Lütticke R., Dettmar R.-J., 2004, *A&A*, 422, 465
- Pohlen M., Dettmar R.-J., Lütticke R., Schwarzkopf U., 2000, *A&AS*, 144, 405
- Press W. H., Teukolsky S. A., Vetterling W. T., Flannery B. P., 1992, *Numerical recipes in C. The art of scientific computing*. Cambridge: University Press, —c1992, 2nd ed.
- Quinn P. J., Goodman J., 1986, *ApJ*, 309, 472
- Quinn P. J., Hernquist L., Fullagar D. P., 1993, *ApJ*, 403, 74
- Read J. I., Lake G., Agertz O., Debattista V. P., 2008, *ArXiv e-prints*, 803
- Robertson B., Bullock J. S., Cox T. J., Di Matteo T., Hernquist L., Springel V., Yoshida N., 2006, *ApJ*, 645, 986
- Robin A. C., Haywood M., Creze M., Ojha D. K., Bienayme O., 1996, *A&A*, 305, 125
- Romano-Diaz E., Faltenbacher A., Jones D., Heller C., Hoffman Y., Shlosman I., 2006, *ApJ*, 637, L93
- Sellwood J. A., 1987, *ARA&A*, 25, 151
- Sellwood J. A., Nelson R. W., Tremaine S., 1998, *ApJ*, 506, 590
- Seth A. C., Dalcanton J. J., de Jong R. S., 2005, *AJ*, 130, 1574

Soubiran C., Bienaymé O., Siebert A., 2003, *A&A*, 398, 141

Springel V., 2005, *MNRAS*, 364, 1105

Springel V., White S. D. M., 1999, *MNRAS*, 307, 162

Stewart K. R., Bullock J. S., Wechsler R. H., Maller A. H., Zentner A. R., 2007, *ArXiv e-prints*, 711

Stoehr F., 2006, *MNRAS*, 365, 147

Toomre A., 1964, *ApJ*, 139, 1217

Tormen G., 1997, *MNRAS*, 290, 411

Tóth G., Ostriker J. P., 1992, *ApJ*, 389, 5

Tsikoudi V., 1979, *ApJ*, 234, 842

Vallenari A., Pasetto S., Bertelli G., Chiosi C., Spagna A., Lattanzi M., 2006, *A&A*, 451, 125

van der Kruit P. C., 1984, *A&A*, 140, 470

van der Kruit P. C., Searle L., 1981a, *A&A*, 95, 105

—, 1981b, *A&A*, 95, 116

van Dokkum P. G., Peletier R. F., de Grijs R., Balcells M., 1994, *A&A*, 286, 415

Velázquez H., White S. D. M., 1999, *MNRAS*, 304, 254

Veltz L., Bienaymé O., Freeman K. C., and collaborators., 2008, *A&A*, 480, 753

Walker I. R., Mihos J. C., Hernquist L., 1996, *ApJ*, 460, 121

Wechsler R. H., Bullock J. S., Primack J. R., Kravtsov A. V., Dekel A., 2002, *ApJ*, 568, 52

Yoachim P., Dalcanton J. J., 2005, *ApJ*, 624, 701

—, 2006, *AJ*, 131, 226

Younger J. D., Besla G., Cox T. J., Hernquist L., Robertson B., Willman B., 2008, *ApJ*, 676, L21

APPENDIX A: SETTING UP THE INITIAL CONDITIONS FOR THE HOST AND SATELLITE SYSTEMS

A1 Main disk galaxy

The main disk galaxy is a self-consistent two-component system, containing a dark matter halo and a stellar disk.

A1.1 Dark Matter Halo

The dark matter (DM) halos in our simulations follow a NFW mass density profile (Navarro, Frenk, & White 1997, hereafter NFW):

$$\rho_{NFW}(r) = \frac{\rho_s}{(r/r_s)(1+r/r_s)^2} \quad (\text{A1})$$

where ρ_s is a characteristic scale density and r_s a scale radius. The advantage of using this density profile is that it is consistent with cosmological simulations, and its evolution with redshift (or time) is relatively well-known (e.g., Wechsler et al. 2002). This implies that it is easy to re-scale its properties to study the formation of thick disks at redshifts greater than zero.

In this paper we adopt a flat cosmology defined by $\Omega_m(z=0) = 0.3$ and $\Omega_\Lambda = 0.7$ with a Hubble constant of $H(z=0) = 70$ km/s/Mpc.

The virial radius of the halo $R_{vir}(z)$ is defined as the radius within which the mean density is $\Delta_{vir}(z)$ times the critical density $\rho_c(z)$ of the universe at a given redshift:

$$M_{vir}(z) = \frac{4\pi}{3} \Delta_{vir}(z) \rho_c(z) R_{vir}^3 \quad (\text{A2})$$

where the virial overdensity $\Delta_{vir}(z)$ is taken from the solution to the dissipationless collapse in the spherical top-hat model. Its value is $18\pi^2$ for a critical universe but has a dependency on cosmology. In the case of flat cosmologies, $\Delta_{vir}(z) \approx (18\pi^2 + 82x + 39x^2)$, where $x = \Omega(z) - 1$, and $\Omega(z)$ is defined as the ratio between mean matter density and critical density at redshift z . Another important related quantity is the concentration c defined as $c = R_{vir}/r_s$. From Wechsler et al. (2002) we take the relation linking M_{vir} to the concentration parameter c at redshift $z=0$ as:

$$c \simeq 20 \left(\frac{M_{vir}}{10^{11} M_\odot} \right)^{-0.13} \quad (\text{A3})$$

We follow Wechsler et al. (2002) to scale both the virial mass of the halo and its concentration as a function of redshift:

$$M_{vir}(z) = M_{vir}(z=0) \exp(-2a_c z), \quad (\text{A4})$$

$$c(z) = \frac{c(z=0)}{1+z} \quad (\text{A5})$$

where a_c is a constant defined as the formation epoch of the halo, taken as $a_c = 0.34$. In practice this means that the structure of the halo of the main galaxy at any redshift is fully determined by imposing only a value for the virial mass at redshift $z=0$. The values of the halo parameters used in our simulations are included in the Table 1.

Since the mass of a NFW profile formally diverges with radius, we introduce an exponential truncation starting at R_{vir} and decaying on a scale r_{dec} (Springel & White 1999):

$$\rho(r) = \frac{\rho_s}{c(1+c)^2} \left(\frac{r}{R_{vir}} \right)^\epsilon \exp\left(-\frac{r-R_{vir}}{r_{dec}}\right) (r > R_{vir}) \quad (\text{A6})$$

where r_{dec} is a free parameter. By requiring continuity at R_{vir} between Eqs. (A1) and (A6), and also between their logarithmic slopes, the exponent ϵ is computed as:

$$\epsilon = -\frac{1-3c}{1+c} + \frac{R_{vir}}{r_{dec}}. \quad (\text{A7})$$

Note that for $r_{dec} = 0.1R_{vir}$ the total mass of the halo becomes $\sim 10\%$ larger than M_{vir} . We define the maximum extension of the halo as $R_{max} = R_{vir} + 3r_{dec}$.

We also allow the contraction of the halo in response to the formation of a stellar disk in its central part (Blumenthal et al. 1986; Mo et al. 1998) The adiabatic contraction first assumes that the gas (that later forms the disk/bulge) is distributed in the same way as the dark matter. Then both the spherical symmetry of the halo and also the angular momentum of each dark matter orbit are conserved during the contraction, i.e.,:

$$r_i M_i(r_i) = r_f M_f(r_f) \quad (\text{A8})$$

where r_i and r_f are the initial and final radius of a shell of dark matter, M_i is the initial total mass (distributed according to an NFW profile) and M_f is the mass distribution after the disk has been formed, and also includes the contribution of the disk. Therefore,

$$M_f(r_f) = M_d(r_f) + (1-m_d)M_i(r_i) \quad (\text{A9})$$

where $m_d = M_{disk}/M_{halo}$. The final dark matter distribution of the adiabatically concentrated halo will be:

$$M_{halo}(r) = M_f(r) - M_{disk}(r). \quad (\text{A10})$$

Now that the mass distribution of the halo component has been defined, it is straightforward to initialise the positions of the particles in our halos. As the next step, the velocity of each particle is computed from the distribution function (DF) associated to the adiabatically contracted mass density profile $\rho_{halo}(r)$. We follow Kazantzidis et al. (2004) and compute numerically the DF that, in general, is given by⁵:

$$f(Q) = \frac{1}{\sqrt{8\pi^2}} \left[\int_0^Q \frac{d^2 \rho_{halo}}{d\psi^2} \frac{d\psi}{\sqrt{Q-\psi}} + \frac{1}{\sqrt{Q}} \left(\frac{d\rho_{halo}}{d\psi} \right)_{\psi=0} \right] \quad (\text{A11})$$

(Binney & Tremaine 1987) where $Q = \psi - v^2/2$; $\psi = -\Phi(r)$ is the effective gravitational potential (including the disk); and v is the velocity of each particle. Finally, we use the rejection method (Press et al. 1992) to generate the velocities for our particles.

A1.2 Stellar Disk

The disk component is constructed following the procedure outlined by QHF93 and Hernquist (1993) which consists, briefly, in initialising particle positions according to a density profile of the form:

$$\rho_d(R, z) = \frac{M_d}{8\pi R_D^2 z_0} \exp\left(-\frac{R}{R_D}\right) \text{sech}^2\left(\frac{z}{2z_0}\right) \quad (\text{A12})$$

where M_d is the disk mass, R_D is the exponential scale-length, and z_0 is the exponential scale-height.

The velocity components v_R , v_ϕ and v_z of the disk particles are calculated from moment equations of the collisionless Boltzmann equation (CBE) supplemented by observational constraints (Binney & Tremaine 1987). We assume that locally (at each point in the disk) the velocity distribution can be approximated by a Maxwellian, whose parameters are set up as follows:

- The radial velocity dispersion $\overline{v_R^2}(R) \propto \exp(-R/R_D)$. This is motivated by observations of external galaxies (van der Kruit & Searle 1981a; Lewis & Freeman 1989). The normalisation constant is set by adopting a certain value of the stability Q-parameter (Toomre 1964) at a particular location in the disk. In this paper $Q = 2$ at $R = 2.4R_D$, which for a Milky Way-like disk corresponds to the solar radius.

- The vertical velocity dispersion $\overline{v_z^2}(R) = 2\pi G\Sigma(R)z_0$, following the isothermal sheet model.

- The dispersion in the azimuthal direction is obtained by using the epicyclic approximation (Binney & Tremaine 1987) $\sigma_\phi^2(R) = \overline{v_R^2}(R)\kappa^2(R)/4\Omega^2(R)$, where κ and Ω are the epicyclic and angular frequencies, respectively. The mean values of the azimuthal Gaussian distributions are calculated from the second moment of the CBE,

$$\overline{v_\phi^2}(R) = \overline{v_R^2}(R) \left[1 - \frac{\kappa^2(R)}{4\Omega^2(R)} - 2\frac{R}{R_D} \right] + v_c^2(R),$$

⁵ For a spherical non-rotating system.

where $v_c(R) = R\Omega(R)$ is the circular velocity considering all the components of the system.

Note that velocities derived from the CBE are close but not identical to the ones derived from the DF of the disk. Unfortunately, the DF is unknown for the disk in Eq. (A12). Therefore, we can expect some initial evolution in the disk properties. As shown in §A3, this evolution is indeed minimal.

A2 Numerical Parameters

The N -body systems are evolved using Gadget-2.0 (Springel 2005) a well documented massively parallel TreeSPH code. Depending on the system under study, this code has to be provided with suitable values for the so-called numerical parameters, being these: the number of particles N to represent a given component in the system; the softening ϵ of gravitational forces to avoid strong artificial accelerations between particles passing close to each other; and finally the timestep Δt , that controls the frequency at which positions and velocities are computed for each particle. In general, these three parameters set the mass, spatial and time resolution in a numerical simulation. At the moment of defining N , ϵ and Δt the usual problem is that they are interrelated in a complicated way. For instance, N will depend on the available CPU power to run the simulations; ϵ will depend on both N and the mass distribution of the system to be simulated; and Δt will depend on the smallest spatial resolution that is possible to resolve, ϵ , and again on the available CPU power. The optimal choice of these parameters will establish a compromise between quality and efficiency in a numerical simulation.

A2.1 Number of particles

Tables 1 and 2 list the numbers of particles used for each component in our simulations. As shown by WMH96, using self-consistent simulations of an isolated halo-disk system, large numbers of particles in the halo are needed to suppress the formation of bar perturbations in the disk. This is because large N_{halo} decreases the graininess of the potential, which bars are seeded from. WMH96 suggest the use of ~ 500000 particles in the halo in order to smooth out the potential for time scales comparable to the orbital decay of satellites in our simulations.

For our purposes, bars are an unwanted effect because they represent an additional source of disk heating, besides the one of interest here. Although the complete elimination of bar formation in a self-consistent simulation is difficult, its effect on the disk can be constrained by evolving the main disk galaxy in isolation, for the same timescale as the merger simulation.

The number of particles in the host disk $N_{host,disk} = 10^5$, and is similar to previous studies on disk heating by mergers with satellites. The satellites are modeled with a relatively large number of particles (particularly in comparison to previous works) to study the distribution of the debris, which is the focus of Paper II. In all cases we can follow accurately the structure and evolution of each component during the simulations.

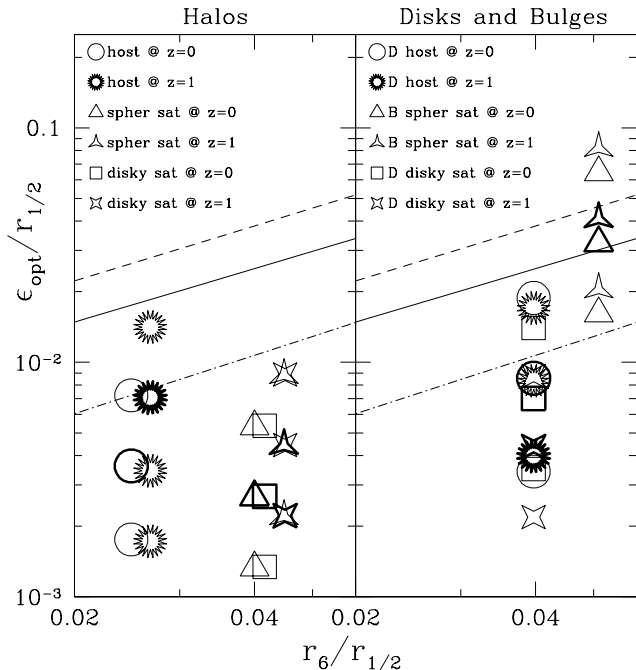


Figure A1. Numerical softening as a function of the mean distance from each particle to the 6th closest neighbour in units of the half-mass radius $r_{1/2}$. Straight lines are extrapolations towards smaller r_6 taken from the results of Athanassoula et al. (2000) [see Fig. 11 in that work]. Dashed, solid and dot-dashed lines show the values for a homogeneous, Plummer and Dehnen sphere (with $\gamma = 0$), respectively. The symbols indicate the values of softenings explored in this paper for each component. Darker symbols show the optimal softenings that produced the best stability in each case.

A2.2 Softening

Many studies have been carried out on how to choose the optimal gravitational force softening ϵ in order to faithfully represent the system (see Sellwood 1987, for an excellent review). We use here the prescription by Athanassoula et al. (2000). These authors present a simple method to estimate ϵ for arbitrary mass distributions as a function of the number of particles. The optimal softening ϵ_{opt} is the one that minimises the error in the forces between particles in a system with a given mass distribution. They find a correlation between ϵ_{opt} and the distance $r_{6,mean}$ from every particle to its sixth closest neighbour, which is defined as:

$$r_{6,mean} = \left(N^{-1} \sum_{i=1}^N r_{6,i}^{-1} \right)^{-1} \quad (\text{A13})$$

where $r_{6,mean}$ depends on both the number of particles and the mass distribution. Fig. A1 shows ϵ_{opt} as a function of $r_{6,mean}$ for three mass distributions discussed by Athanassoula et al. (2000) in order of increasing density: homogeneous sphere, Plummer profile and Dehnen model (with $\gamma = 0$). To estimate the ϵ_{opt} for the systems of our simulations the procedure followed is: 1) compute $r_{6,mean}$ for each of our components; 2) compare the central density of our components to the ones of the homogeneous, Plummer and Dehnen spheres. By doing so the optimal softening

for each component can be constrained within a range on the plane $r_6 - \epsilon_{opt}$; and 3) ϵ_{opt} is found by running a few simulations with a set of ϵ within this range and choosing the one that offers the best stability. Specifically, a softening is considered optimal when each component of both the host and satellite systems present the least evolution in their structure and kinematics (in the case of the host minimising the effect of non-axisymmetries) during the amount of time required for the satellite to sink and become fully disrupted.

In Fig. A1 darker symbols show the adopted values of ϵ_{opt} for each component at every redshift. Note that for each component the values of ϵ_{opt} are well constrained on the $r_6 - \epsilon_{opt}$ plane, facilitating the extrapolation of these optimal values to similar systems with a different number of particles. For each component, the adopted values of ϵ_{opt} are listed in Table 1 and Table 2.

The distinctive location of the optimal softenings on the $r_6 - \epsilon_{opt}$ diagram basically depends on both the central concentration of the systems and on the number of particles used to model them. For instance, halos of hosts and satellites at “z=0” and “z=1” always lie below the Dehnen model because they are more centrally concentrated (even more so when the adiabatic contraction is taken into account). On the other hand, the separation along the r_6 -coordinate between the optimal softening of the halos of hosts and satellites reflects the difference in the number of particles used to model them. In this sense it is easy to associate systems with a larger number of particles to smaller mean distances between particles and viceversa, given that the systems are compared in a normalised scale.

Also note that the disk satellite requires a halo that is better resolved at “z=1” than for a spherical satellite in order to reach the best stability. This can be explained by the fact that a better resolved centrally concentrated region of the halo is able to inhibit the formation of non-axisymmetries (e.g., see Athanassoula et al. 2005).

In order to check the robustness of our choices of both number of particles and softenings, we have followed the suggestion by the referee and also simulated one of the “z=1” experiments adopting the same mass and softening for the stars in the satellite and in the host disk stars. Reassuringly we found practically no difference in the global properties of the final thick disk in comparison to our “standard” choice of numerical parameters.

A2.3 Timestep

The timestep Δt has been defined for our simulations according to the standard criterion of Gadget-2.0. This means that the timestep for each particle is calculated as $\Delta t = \sqrt{2\eta\epsilon/|\mathbf{a}|}$, where η is a dimensionless parameter controlling the accuracy of the timestep criterion, ϵ is the softening associated to each particle, and \mathbf{a} is the gravitational acceleration suffered by each particle. Δt is also limited by a maximum value in order to prevent particles having too large timesteps. The maximum timestep is defined as a few percent of the timescale $t_c = 2\pi\epsilon/V_c(\epsilon)$ calculated for the component that has the smallest ϵ in the system, where V_c is the circular velocity. This ensures us that we follow the evolution of even the smallest components in the system with enough time resolution. We have set $\eta = 0.025$ and the maximum timestep to 0.25 Myr, which give us typical con-

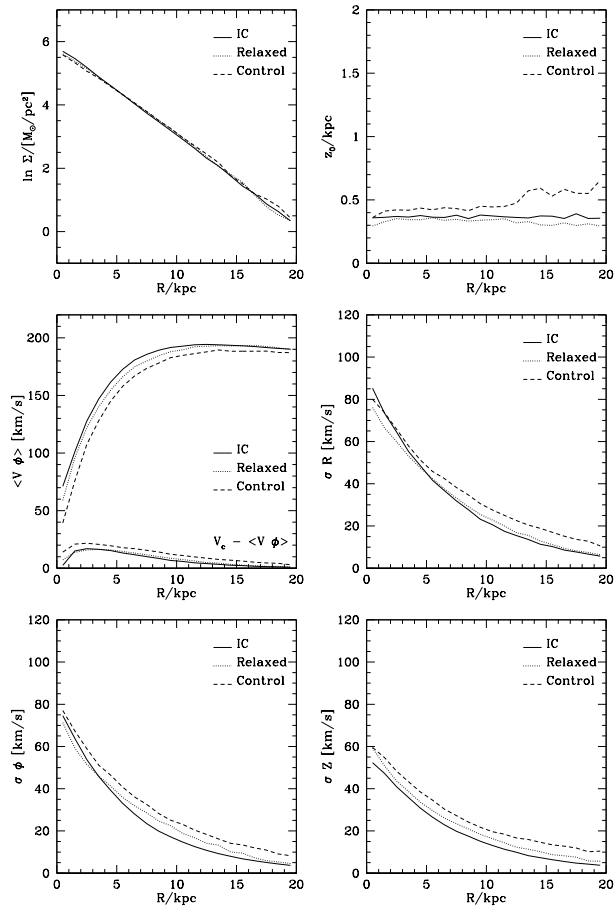


Figure A2. Evolution of the structural and kinematic properties of the isolated host disk, for the “ $z=0$ ” configuration. The solid lines show the initial conditions. The dotted lines show the disk after 1 Gyr of evolution within the fixed halo potential. The dashed lines show the disk’s evolution after 5 Gyr within the N -body halo. The latter model is used as the control case in the comparison to the minor merger simulations. A similar behaviour is obtained for the disk in the “ $z=1$ ” configuration.

servations of energy and angular momentum that are better than 0.1% over 9 Gyr of evolution for our main disk galaxy configured at “ $z=0$ ”.

A3 Evolution of Isolated Host

To test the stability of the host galaxy, this is simulated in isolation, i.e. in the absence of any external perturbation.

We first relax the disk component within a “rigid version” of the halo potential (which mimics the N -body halo described in §A1.1) for a few rotational periods (normally 1 Gyr). Once the disk component is relaxed (i.e., there are no further changes in either its morphological or kinematical properties) the “rigid” halo is simply replaced by its N -body (“live”) counterpart, and evolved for additional 5 Gyr in isolation for the configuration at “ $z=0$ ”, and during 4 Gyr for that at “ $z=1$ ”. As described in §3.1, these time windows are enough to study the merger events that are of interest to us. Strong bar instabilities appear in the host galaxies evolved

in isolation only after 9 Gyr and 7 Gyr for the configurations at “ $z=0$ ” and “ $z=1$ ”, respectively.

Fig. A2 shows how the initial properties of the host disk at “ $z=0$ ” change after being relaxed within a fixed halo for 1 Gyr, and after 5 Gyr in the live halo. Its properties are measured in concentric rings of 1 kpc of width, including particles out to ~ 15 initial scale-heights. The surface density profiles $\Sigma(R)$ (top left panel) indicate that the scale-lengths of the disks (given by the inverse of the slope in log-linear scale) stay practically unchanged. Similarly, the vertical structure of the disk does not show significant evolution (top right panel), except a moderate amount of flaring in the outer disk, which are due to spiral instabilities induced by swing-amplified Poisson noise in the disk. The scale-heights, measured at $R = 2.4R_D$, change from $z_0 = 0.35$ kpc to 0.41 kpc in the “ $z=0$ ” configuration and from 0.17 kpc to 0.24 kpc in the “ $z=1$ ” one. The disks are also slightly slowed down (middle left panel), while the velocity dispersions show an increase of ~ 5 km/s in the first Gyr in the fixed halo, and a total of < 10 km/s after 5 Gyr of evolution in the live potential (middle-right and bottom panels). The velocity ellipsoid of the disk (also measured at $R = 2.4R_D$) increases from $(\sigma_R, \sigma_\phi, \sigma_Z) = (28, 20, 17.5)$ km/s to $(35, 28, 24)$ km/s in the “ $z=0$ ” configuration and from $(25, 18, 14)$ km/s to $(32, 28, 22)$ km/s in the “ $z=1$ ” one.